Bioactive Materials 27 (2023) 181–199

Contents lists available at ScienceDirect

Bioactive Materials

journal homepage: www.keaipublishing.com/en/journals/bioactive-materials

An engineered lamellar bone mimicking full-scale hierarchical architecture for bone regeneration

Tao Yang [a,1], Zhichao Hao [a,1], Zhenzhen Wu [b,1], Binxin Xu [a], Jiangchen Liu [a], Le Fan [a], Qinmei Wang [c], Yanshan Li [a], Dongying Li [a], Sangzhu Tang [a], Chuanzi Liu [a], Weichang Li [a,**], Wei Teng [a,*]

[a] Hospital of Stomatology, Guanghua School of Stomatology, Sun Yat-sen University and Guangdong Provincial Key Laboratory of Stomatology, No.56, Lingyuan West Road, Yuexiu District, Guangzhou, 510055, China
[b] Department of Periodontology and Implantology, Stomatological Hospital, School of Stomatology, Southern Medical University, Guangzhou, China
[c] Laboratory of Biomaterials, Key Laboratory on Assisted Circulation, Ministry of Health, Cardiovascular Division, The First Affiliated Hospital, Sun Yat-sen University, Guangzhou, China

ARTICLE INFO

Keywords:
Full-scale hierarchy
Lamellar bone
Bioskiving
Mineralization
Integrin α5-PI3K/AKT signaling Pathway

ABSTRACT

Lamellar bone, compactly and ingeniously organized in the hierarchical pattern with 6 ordered scales, is the structural motif of mature bone. Each hierarchical scale exerts an essential role in determining physiological behavior and osteogenic bioactivity of bone. Engineering lamellar bone with full-scale hierarchy remains a longstanding challenge. Herein, using bioskiving and mineralization, we attempt to engineer compact constructs resembling full-scale hierarchy of lamellar bone. Through systematically investigating the effect of mineralization on physicochemical properties and bioactivities of multi-sheeted collagen matrix fabricated by bioskiving, the hierarchical mimicry and hierarchy-property relationship are elucidated. With prolongation of mineralization, hierarchical mimicry and osteogenic bioactivity of constructs are performed in a bidirectional manner, i.e. first rising and then descending, which is supposed to be related with transformation of mineralization mechanism from nonclassical to classical crystallization. Construct mineralized 9 days can accurately mimic each hierarchical scale and efficiently promote osteogenesis. Bioinformatic analysis further reveals that this construct potently activates integrin α5-PI3K/AKT signaling pathway through mechanical and biophysical cues, and thereby repairing critical-sized bone defect. The present study provides a bioinspired strategy for completely resembling complex hierarchy of compact mineralized tissue, and offers a critical research model for in-depth studying the structure-function relationship of bone.

1. Introduction

Bone is the highly hierarchical and mineralized tissue. The hierarchical architecture of bone is divided into 9 levels [1], ranging from the major components, i.e. nano-hydroxyapatite (nHA) and collagen, to the whole bone. This extremely sophisticated multi-scale hierarchy is ultimately responsible for the bioactive functionality and mechanical trait of bone [2,3]. Nowadays, millions of the bone grafting procedures were performed every year. Due to the donor site morbidity of autograft as well as pathogen transmission risk of allograft and xenograft [4], engineering bone construct emerges as a promising avenue to fulfill the increasing demand for valid bone grafting in clinic. Driven by the growing desire for superior bone regeneration, engineered bone constructs with desirable performance are urgently needed. Since hierarchical biomimicry is the foundation of functional biomimicry, simulating full-scale hierarchy of bone is believed to be a promising tactics to function as extracellular matrix presenting both physicochemical and mechanical cues for stem cell attachment, proliferation and osteogenic differentiation [5–9]. In the recent years, much effort has been devoted to simulating bone hierarchy and promising progress has

Peer review under responsibility of KeAi Communications Co., Ltd.
* Corresponding author.
** Corresponding author.
E-mail addresses: liwch57@mail.sysu.edu.cn (W. Li), tengwei@mail.sysu.edu.cn (W. Teng).
[1] These authors contributed equally to this work.

https://doi.org/10.1016/j.bioactmat.2023.03.024
Received 11 December 2022; Received in revised form 20 February 2023; Accepted 30 March 2023

been made [10–12]. To date, most studies, however, focus on engineering low-level disordered hierarchy [13–15], which is reminiscent of immature woven bone rather than mature form commonly employed in bone grafting operations [16,17].

The mature bone, cortical and trabecular bone, is characterized by high-level hierarchy formed by orderly and densely packed lamellar bone [1]. Consequently, imitating lamellar bone is the prerequisite in engineering bone constructs with splendid performance to treat defected bone in clinics. Likewise, lamellar bone exhibits an intricate and ordered hierarchy [18,19]: numerous poorly crystalline carbonated nHA are selectively distributed within collagen fibril (level I) to form mineralized collagen fibril (level II). Numerous mineralized collagen fibrils are assembled into arrays (level III), which are further parallelly aligned and formed so-called unidirectional pattern (level IV). Subsequently, arrays are tightly packed into bundle and plentiful bundles are aligned side-by-side. The generated extensive sheet of parallel bundles (level V) is named as bone lamella, of which thickness is only 2–16 μm [20]. Furthermore, dozens of bone lamellae are arranged in an alternating stacking manner to produce lamellar bone (level VI), where parallel bundles are periodically rotated, e.g. oriented orthogonally, between adjacent lamellae [21]. The compacted and complicated hierarchy of lamellar bone is often described as the twisted plywood motif.

Numerous attempts have been made to imitate the hierarchy of lamellar bone [22]. Unfortunately, engineered lamellar bones still have limitations in terms of mechanical and osteogenic performance. Failure to accurately mimic the full-scale hierarchy is the predominant cause and stands as a daunting challenge. Noteworthy, all the hierarchical scales of lamellar bone, from molecular constituent to microscale, plays pivotal roles. nHA is featured by excellent osteoconduction. Collagen can favor cell attachment [23] and further self-assemble into fibrils, serving as the crucial template for nHA deposition and orientation [24]. The high elastic modulus of mineralized collagen fibril endows bone with inherent mechanical property, and in conjunction with its unique topology induces the osteogenic differentiation of bone marrow mesenchymal stem cells (BMSCs) [25]. The unidirectional alignment of bone lamella is conducive to furnishing favorable space for cytoskeleton reorganization and cell differentiation [26,27]. The twisted plywood architecture of lamellar bone is advantageous to improving the isotropy of mechanical trait and functioning as the barrier for microcrack propagation [28–30].

Nowadays, mineralization following self-assembly of collagen (MFS) has been evidenced to be an effective approach mimicking bone hierarchy, in which collagen-based matrix is first self-assembled in vitro followed by mineralization based on amorphous calcium phosphate (ACP) [31,32]. Thereinto, mineralization is of vital importance to simulating micro- and nanostructure of bone, while the framework is primarily determined by pertinent collagen matrix. Thus far, despite that collagen hierarchy of lamellar bone has been simulated to a certain extent via various approaches [33], the full-scale simulation cannot yet be accomplished. The possible reason is that current techniques are principally based on bottom-up strategy, in which partial collagen denaturation is inevitable following extraction process [34], and more importantly, the arrangement of the collagen fibrils cannot be precisely controlled during self-assembly [35]. Consequently, the unidirectional pattern, bundles of arrays, thickness of collagen lamella and periodic rotation between lamellae cannot accurately resemble those of lamellar bone, leading to the inferior mimicry.

Bioskiving is a sectioning-based fabrication technique to engineer collagen matrix. Guided by top-down strategy, bioskiving directly sections decellularized tendon into collagen sheets via microtome. Through further procedure of stacking or rolling collagen sheets, 2D or 3D collagen matrix with complicated hierarchy can be fabricated [36]. These 2D and 3D collagen matrices fabricated by bioskiving scaffolds have been widely used in the field of tissue engineering [36–39], such as tuning cell alignment, facilitating the regeneration of peripheral nerve and participating in the construction of biomimetic blood vessel. Since bioskiving directly utilizes decellularized tendon to fabricate collagen matrix, the drawbacks related with current techniques of engineering collagen matrix based on bottom-up strategy are supposed to be addressed [40,41]. For example, potential collagen denaturation during extraction is avoided. Meanwhile, the striated nanostructure of collagen fibril, arrays of fibril and parallel alignment pattern of native tendon are highly retained [38]. The mechanical strength of the collagen constructs derived from tendon sheet is stronger than that from reconstituted collagen. The thickness of collagen sheet can be exactly controlled to only a few microns by microtome. More significantly, a compact and multi-sheeted collagen construct can be fabricated through sectioning and stacking procedure, and the orientation of each stacked sheet can be precisely manipulated during stacking process. We found that this multi-sheeted construct shares strong similarity with the collagen matrix of lamellar bone. Hence, we hypothesize that the conundrum replicating full-scale hierarchy of lamellar bone can be addressed through using bioskiving.

Another key issue involving in MFS is mineralization, which determines the mimicry of micro- and nanostructure of biomimetic bone and further exerts a significant effect on bioactivity. Of note, the majority of investigations so far have focused on mineralizing individual collagen fibrils or loosely arranged fibrils in the form of porous collagen scaffolds, in which ACP could easily infiltrate and achieve mineralization of whole collagen scaffolds. However, whether ACP could penetrate the full-thickness of densely packed collagen matrix and efficiently mineralize collagen fibrils are rarely reported. The architecture of surface and internal region of compact collagen matrix following mineralization remains to be explored. Mineralization can exert a considerable impact on hierarchical biomimicry and further affect functional biomimicry of construct. Therefore, the effect of mineralization on hierarchy of engineered lamellar bone should be systematically elucidated.

Recognizing the major bottleneck in mimicking lamellar bone, i.e. how to precisely simulate its full-scale hierarchy, this study represents our attempt to address the structure-related-dilemma via combinatory application of bioskiving and mineralization. Through bioskiving, a series of multi-sheeted constructs were built and then mineralized by ACP. The influence of mineralization on the physicochemical traits and bioacitvities of compact constructs was systematically explored in this study. Thereinto, the hierarchy-bioactivity relationship and the potential mechanism of osteogenic bioactivity were investigated. Furthermore, critical sized bone defect model was employed to evaluate the repairing performance in vivo. This study offers a novel avenue for mimicking full-scale hierarchy of mature bone. Through this method, more complex hierarchical structure of bone (e.g. osteon) with superior bioacitvity could be fabricated, paving the way to eventual construction of biomimetic whole bone.

2. Materials and methods

2.1. Fabrication and characterization of biomimetic collagen matrix (BCM) of lamellar bone

2.1.1. Decellularization treatment of tendon and characterization

Decellularized bovine tendons were first prepared to serve as the fabrication material for bioskiving. Based on the previous approach with some modification [42], Fresh bovine tendons were harvested from the local slaughter house within 4 h of sacrifice and immediately kept in ice during the delivery to the laboratory. The tendon part from the musculotendinous junction to the osseous insertion was separated and the sheaths surrounding tendon were removed from tendons. The tendons were cut into blocks (roughly 20 mm × 20 mm × 5 mm) and shaken in the decellularization solution (1 mM Tris buffer, 1% w/v SDS and 0.1 mM EDTA) for 72 h. The decellularization solution was changed every 24 h. Then, the tendon blocks were thoroughly washed with deionized water prior to immersing in DNAse I solution (1 mg/mL) for 24 h,

followed by gradient dehydration and drying under vacuum.

To verify decellularization treatment has remarkably diminished tendon derived cells and intactly preserved collagen, the following investigations were conducted. Immunofluorescence staining was first performed. Briefly, tendon blocks were fixed with 4% paraformaldehyde and blocked with 5% bovine serum albumin (BSA) for 2 h. Then, specimens were incubated with Cy5-*anti*-collagen (1:50, Guangrui biotech., China) at 4 °C overnight prior to stained with dihydrochloride (DAPI, Invitrogen, USA) and observed by confocal laser scanning microscope (CLSM, Olympus FV3000). Collagen content was quantified using a Hyp assay kit (Keygen, China). Lyophilized tendon blocks were hydrolyzed with hydrochloric acid at 100 °C for 20 min and neutralized by sodium hydroxide. The absorbance was measured at 570 nm on by spectrophotometer (Bio-Rad). The Hyp levels were determined based on standard curve. The collagen content was calculated using a Hyp-to-collagen ratio of 1:7.2 and was normalized to the initial dry weight of tendon. Additionally, The DNA content of tendon was measured. Lyophilized tendon blocks were cut and digested with proteinase K and RNase A (TaKaRa, China) for 4 h. The nucleic acid was extracted according to the instruction. The DNA concentration was quantified by spectrophotometer. The DNA content was normalized to the initial dry weight of tendon. Furthermore, to guarantee the decellularized tendon has thoroughly removed toxic agents (SDS and EDTA), the cytotoxicity was conducted via testing the extracted medium of decellularized tendon. The extracted media were obtained by immersing the decellularized tendon in DMEM with 10% FBS and 1% penicillin/streptomycin at 37 °C. The ratio of tendon to media was 0.1 g/mL. L929 cells were seeded in 96-well plate at a density of 5000. After 1 d, the extracted medium was filtered by 0.1 μm filter and added to well plated at different concentrations (25%, 50% and 100%). 1 and 2 days later, the media were aspirated and 150 μL culture media containing 20 μL CCK8 (Dojindo, Japan) were added. The absorbance was measured at 450 nm by plate reader (Beckman Coulter AD 340). L929 cells treated with no extracted media were set as control.

2.1.2. Construction of BCMs via bioskiving and hierarchical characterization

Construction of BCMs via bioskiving involved sectioning and stacking procedures. The detailed process was illustrated in Fig. S1. Briefly, extremely dried decellularized tendon blocks were embedded in OCT compound and sectioned in the direction parallel to fibrils via the cryomicrotome (CM1950). The thickness of collagen sheets was set as 10 μm. To remove the residual OCT compound, collagen sheets were repeatedly washed in 75% ethanol and deionized water in sequence. To guarantee collagen sheet is fully expanded and reduce the potential fissure inside BCM, the stacking procedure of collagen sheets was conducted in water environment. The first collagen sheet was attached to a polytetrafluoroethylene plate. Then, the second collagen sheet was stacked above the first collagen sheet with fibril orientation rotating at 90^{o}. Following this mode, 20 collagen sheets was stacked and 200 μm-thickness BCM was constructed. The BCM was completely dried in air at room temperature. Dehydration could decrease the spacing between collagen molecules and generate vast hydrogen bond between collagen sheets, facilitating the construction of stable and compact BCM. Finally, dried BCM was peeled away from polytetrafluoroethylene plate and trimmed.

The hierarchical structure of BCMs was examined by monitoring the surface and cross-section of BCMs. To prepare the cross-section of BCMs, BCMs were embedded and cryo-sectioned along the direction perpendicular to the sheet. The specimens were washed, dehydrated in gradient ethanol solution and mounted on the quartz substrate. For the investigation of scanning electron microscopy (SEM, Quanta 400F), specimens were sputter-coated with gold particles and captured at the accelerating voltage of 15 kV. For the inspection of the LSCM profilometer (LSM700), the specimens were scanned at 405 nm and analyzed at the ortho-mode. In addition, to verify that collagen in BCM was not denatured, the investigation of circular dichroism (CD) and differential scanning calorimetry (DSC) were conducted. Gelatin, the denatured form of collagen, was employed as the control group. As for CD measurement, 0.4 mg/mL BCM and gelatin solution were obtained by dissolving BCM and gelatin in 0.1 mol/L hydrochloric acid. The BCM and gelatin solution were equilibrated for 1 h prior to test by Chirascan Plus spectropolarimeter (Applied Photophysics). The spectra were documented from 190 to 240 nm. As for DSC measurement, the analyses of BCM and gelatin were investigated by DSC (DSC-204 F1). The test was performed in the nitrogen atmosphere. The temperature was set from 100 °C to 120 °C.

2.2. Construction and physicochemical characterization of biomimetic lamellar bone (BLB)

2.2.1. Fabrication of BLBs through mineralizing BCMs

BLBs were constructed based on MFS strategy. ACP mineralization solution was prepared according to our previously described method [43,44]. In brief, 330 mg K_2HPO_4 was completely dissolved in Tris buffer containing 10% (w/v) carboxymethyl chitosan (Xiya Reagent Co., China). 10 mL Tris buffer containing 264 mg $CaCl_2$ was added drop by drop, followed by stirring for 30 min. Then, BCMs were immersed in ACP solution at 37 °C under shaken condition. The mineralization solution was refreshed every 3 d. At 6 d, 9 d and 12 d, BLBs were taken out and thoroughly washed to remove the loosely attached minerals before drying. BLBs were named according to the mineralization time (BLB6d, BLB9d and BLB12d). BLBs were sterilized by ethylene oxide prior to further characterization.

2.2.2. Physicochemical characterization of BLBs

To elucidate the effect of mineralization time on the hierarchical biomimicry of BLBs, the following characterizations were conducted. The macroscale alteration of BCM, BLB6d, BLB9d and BLB12d were documented through digital camera. In addition, constructs were incubated with Alizarin Red S for 3 min followed by washing and image capture to evaluate mineral formation. To investigate the nano-hierarchy of BLBs, transmission electron microscopy (TEM, FEI Tecnai G2 Spirit) was conducted. BLBs were pulverized in liquid nitrogen prior to dropping onto the 300 mesh copper grids. The accelerating voltage was set as 120 kV. The micro-hierarchy of BLBs was evaluated by SEM at both surface and cross-section. To evaluate whether calcium and phosphorus were spatially distributed throughout BLBs, elemental mapping of energy dispersive spectrum (EDS) was performed at cross-section plane. To investigate the hierarchy of BLB under the physiologically moist environment and to deeply evaluate the mineral distribution, BCM, BLB6d, BLB9d and BLB12d were prewetted in PBS for 30 min. Then, excessive water was removed by tissue paper and constructs were scanned by micro-CT (lCT 80; Scanco Medical, Switzerland). During micro-CT scanning, constructs were kept in moist condition. The parameters of micro-CT were set as the following: voltage 70 kV, electric current 114 μA and resolution 3 μm. 10 random transverse sections of micro-CT image were selected. The construct in each transverse section was equally divided into three regions (illustrated in Fig. 3B(b)): the surface region at both side and the internal region, of which HU values were measured by Mimics Research 20.0 software. In addition, the surface roughness of the BLBs was detected by LSCM profilometer and analyzed at the Gauss-mode.

To further evaluate the influence of mineralization time on the physicochemical properties of BLBs, the following investigations were performed. The surface wettability of BLBs were measured by contact angle goniometer (Model JY-82). The constructs were stuck onto the glass slide and the profile of a sessile drop of 2 μL of deionized water on the surface of constructs was captured. The intersection angles were documented to calculate average values. Nanoindenter (Keysight G200) was employed to identify the nanomechanical properties of BLBs. The constructs were mounted on stub and the elasticity modulus of BLBs surface was tested. In order to investigate whether the mineral crystals

in surface and internal of BLBs were the same, the lamellae from the surface and internal one-third region of BLBs were separated and pulverized in liquid nitrogen. The crystal structures of different region of BLBs were assessed by X-Ray Diffractometer (XRD, Empyrean). 2θ range was set from 10^o to 60^o and the step size was set as 0.02^o. ATR-FTIR (Nicolet iN10) was performed on BCM, BLB6d, BLB9d and BLB12d to assess the chemical compositions. The spectra were scanned in the range between 400 and 2000 cm^{-1}. The mineral content in BLBs was measured by thermogravimetric analysis (TGA, TG209F1 libra) at a heating rate of 10 °C/min from room temperature to 800 °C in the air atmosphere. The HA content was evaluated by the remaining weight at 700 °C after the organics of the construct was completely combusted [45]. The element of constructs was also analyzed by X-ray photoelectron spectroscopy (XPS, Thermo ESCALAB 250XI).

2.3. In vitro osteogenic assay of BLBs

2.3.1. Cell culture

Following evaluating the effect of mineralization time on hierarchical biomimicry of constructs, the relationship between hierarchical mimicry and osteogenic bioactivity was further illuminated. BMSCs were extracted and collected from the femoral marrow of 3-week female Sprague–Dawley rats. Briefly, the femurs and tibias of rats were collected and cleaned, followed by immersed in 10% penicillin/streptomycin, 75% ethanol and PBS for 1 min in sequence. Both ends of femurs and tibias were removed by scissors and the medullary cavity was rinsed to harvest primary BMSCs. Following centrifugation and resuspension, BMSCs were cultured in α-MEM supplemented with 10% FBS and 1% penicillin/streptomycin. BMSCs were grew in T-25 cm^2 flasks at humidified atmosphere at 37 °C and 5% CO_2 and harvested with 0.25% trypsin-EDTA prior to passaging or seeding. BMSCs from fourth passage were used for further biological assay.

BCM, BLB6d, BLB9d and BLB12d were trimmed into circular-shape prior to being placed into well plate, respectively. The constructs were immersed in 75% ethanol for 1 h. Then, the constructs were thoroughly washed by PBS and prewetted in α-MEM culture media before BMSCs seeding.

2.3.2. Immunofluorescent staining

To estimate the toxicity of constructs, live/dead cell double staining was conducted by the live/dead kit (BestBio Science, China). BMSCs were seeded on the constructs placed in 96 well plate at the density of 5000 with 150 μL culture media. The culture media were refreshed every 2 d. At the 1 d, 4 d and 7 d, culture media were aspirated out and BMSCs seeded constructs were gently washed with PBS. Then, BMSCs seeded constructs were stained by calcein-AM for 15 min and PI for 5 min in sequence, followed by gentle PBS washing. The BMSCs seeded constructs were carefully transferred onto slide and observed by CLSM.

Cell morphology was observed by immunofluorescent staining of F-actin. After culturing for 1 d, BMSCs seeded constructs were fixed by 4% paraformaldehyde for 20 min, washed by PBS and permeabilized with 0.1% Triton X-100 for 5 min. Then, BMSCs seeded constructs were incubated with Actin-Tracker Green-488 (Beyotime Institute of Biotechnology, China) for 1 h to stain cytoskeleton. After PBS washing, nuclei were stained by DAPI and cell morphology was investigated by CLSM.

2.3.3. Cell proliferation assay

BMSCs were seeded on BCM, BLB6d, BLB9d and BLB12d placed in 96 well plate at the density of 5000 with 150 μL culture media. At days 3, 7 and 14, cell proliferation was evaluated using the CCK-8 assay kit. The culture media were entirely aspirated and rinsed by PBS three times. Then, 150 μL culture medium containing 20 μL CCK-8 reagent was added and incubated for 3 h. Subsequently, the media were taken out and their optical density (OD) values at 450 nm were detected by plate reader.

2.3.4. Osteogenic differentiation assay

BMSCs were seeded on the constructs placed in 24 well plate at the density of 2×10^4 with 1 mL culture media. 1 day later, the osteogenic culture medium (BMSCs culture medium supplied with 10 nM dexamethasone, 50 μg/mL ascorbic acid and 10 mM β-glycerol phosphate) was added and changed every 2 days. At day 7 and 14, alkaline phosphatase (ALP) activity of BMSCs was tested by ALP assay kit (Beyotime Institute of Biotechnology, China). At day 14 and 21, osteocalcin (OCN) content of BMSCs was investigated by OCN ELISA kit (Mlbio, China).

Real-time reverse transcript polymerase chain reaction (real-time RT-PCR) was applied for gene analysis. After BMSCs were grown on constucts in osteogenic culture medium for 14 days, total RNA (1 μg) was extracted in accordance with the Trizol method (Invitrogen, USA). Reverse transcription was performed using a Hifair II Strand cDNA Synthesis Kit (Yeasen, China) To standardize the alignment temperature, a number of cycles were run for each set of primers. Real-time PCR was performed with a Hieff UNICON Power qPCR SYBR Green Master Mix (Yeasen, China) and sense and antisense PCR primers used are listed in Table 1. We used the GAPDH as a housekeeping gene to correct the tested gene expression.

Based on the results of above-mentioned physicochemical and osteogenic assays, BLB with optimal properties was screened and employed in subsequent animal study and bioinformatic analysis.

2.4. In vivo study of BLB

2.4.1. Rat critical size cranial defect model

After physicochemical and osteogenic characterization in 2.2 and 2.3 section, whether screened BLB with optimal biomimicry could efficiently repair bone defect in vivo was assessed. Both BCM and screened BLB sterilized by ethylene oxide were cut into discs with a diameter of 5 mm and immersed in saline before implantation. The bilateral 5-mm critical sized calvarial defects of Sprague–Dawley rat were established [46]. 14 Sprague–Dawley rats were used and accordingly 28 bone defects were created. 28 bone defects were divided into 4 groups: screened BLB group, BCM group, autograft group and blank (untreated) group. Each group contained 7 samples. The animal study was approved by the Institutional Animal Care and Use Committee, Sun Yat-Sen University (YSU-IACUC-2018-000246). Sprague–Dawley rats (10-week-old, female) were acclimated for 1 week. The rats were administered general anesthesia by intraperitoneal injection of ketamine (100 mg/kg, Yuhan, Korea). The rat was placed in the prone position and immobilized during surgery. The cranium hair was shaved. Next, the longitudinal incision was made along the midline from the nasofrontal to the occipital region to fully exposure dorsal calvarium. Under continuous irrigation with sterile saline, 5 mm diameter full-thickness bone defects were made by stainless-steel trephine at both left and right side of the calvarium. Bone defect was randomly treated as follows: implanted with screened BLB, implanted with BCM, implanted with autogenous bone (the calvarial bone just removed by drill) or untreated (considered as blank). Of note,

Table 1
Primers sequences used for real-time PCR of BMSCs.

Gene		Primer
Runx2	F	CGCCTCACAAACAACCACAG
	R	TGCAGCCTTAAATGACTCGGT
ALP	F	ATGTCTGGAACCGCACTGAAC
	R	AGCCTTTGGGATTCTTTGTCAG
OPN	F	GATGAACAGTATCCCGATGCC
	R	CCCTCTGCTTATACTCCTTGGAC
BSP	F	AGAAAGAGCAGCACGGTTGAGT
	R	GACCCTCGTAGCCTTCATAGCC
OCN	F	ACCCTCTCTCTGCTCACTCTGC
	R	TATTCACCACCTTACTGCCCTCC
GAPDH	F	TTCCTACCCCCAATGTATCCG
	R	CATGAGGTCCACCACCCTGTT

both left and right side of bone defect in the same animal cannot subjected to the same treatment. Following placing constructs in surgical site, soft tissues were repositioned and closely sutured. After 12 weeks, rats were euthanized and the calvaria was fixed in paraformaldehyde for the following analysis.

2.4.2. Micro-CT analysis

The samples were scanned by micro-CT with following parameters: voltage 70 kV, electric current 114 μA and resolution 20 μm. Bone volume fraction (BV/TV) and bone density were investigated to assess the bone regeneration performance of BLB. The three-dimensional images were reconstructed by Mimics Research 20.0 software.

2.4.3. Histological investigation

The fixed calvaria were decalcified in 10% EDTA, followed by dehydrated in graded series of ethanol and embedded in paraffin. The calvarial tissues surrounding the defect were sectioned with 10 μm thickness and stained with haematoxylin-eosin (HE) and Masson's Trichrome (Baso, China) according to standard procedures. Regenerated tissues were observed by light microscopy (Olympus BX51) equipped with Image-Pro Plus software (Azure Biosystems Inc., CA). The immunofluorescent staining was also conducted. Briefly, antigen retrieval was performed by incubating sectioned tissue slides with sodium citrate antigen retrieval solution (HIER buffer, Gene Tech, China) for 15 min. Then, sectioned tissue slides were blocked by 5% BSA for 1 h, and subsequently incubated with primary antibodies against OCN (1:200, Thermofisher) overnight. Alexa Fluor 488 secondary antibody was employed to stain for 1 h. After PBS washing, sectioned tissue slides were stained with DAPI and viewed by CLSM.

2.5. Study of osteogenic mechanism of BLB

2.5.1. RNA sequencing analysis

BMSCs were seeded on BCM and optimal BLB screened by 2.2 and 2.3 section placed in 6 well plate at the density of 6×10^4 with 2 mL culture media for 14 days. RNA was isolated from BMSCs using the TRIzol reagent. RNA sequencing libraries were constructed and further subjected to deep sequencing using the BGISEQ-500RNA seg platform at BGI Genomics (Shenzhen, China). The sequencing data were filtered with SOAPnuke, and a heatmap was drawn using Pheatmap (v1.0.8) according to the gene expression of different samples. Differential expression analysis was performed using DESeq2 (v1.4.5) with a Q value ≤ 0.05. KEGG, GO and GSEA enrichment analyses of annotated differentially expressed genes were performed using Phyper based on the hypergeometric test. Significant levels of terms and pathways were corrected by the Q value with a rigorous threshold (Q value ≤ 0.05) by Bonferroni correction.

2.5.2. Western blotting

Total protein was collected with a total protein extraction kit (Beyotime Institute of Biotechnology, China) and centrifuged at 12,000 rpm at 4 °C for 15 min. The supernatant was collected and stored at −80 °C for detection. After quantitatively measured by the BCA method, all the samples containing 30 μg protein were separated on 6% and 10% SDS-polyacrylamide gels, and electro-transferred transferred onto polyvinylidene difluoride membranes. The membranes were incubated for 1 h with 5% BSA in PBS buffer to block non-specific protein binding. Subsequently, the membranes were incubated with primary antibodies against integrin α5 (ITGα5), phosphorylated-AKT (p-AKT) and GAPDH (All Cell Signaling Technology, USA) at 4 °C overnight, washed with TBST and probed with a horseradish peroxidase-conjugated secondary antibody for 1 h at room temperature. Finally, the blots were detected by enhanced chemiluminescence Western Blot detection kit (Milipore, USA). Band intensities ratio of phosphorylated form to total form were analyzed Image Lab software (Bio-Rad, USA). Results were reproduced in 3 independent experiments with different samples.

2.5.3. Histological immunofluorescent staining

To verify the signaling pathway, histological sections of animal were immunofluorescently stained. Antigen retrieval was first conducted by incubating sectioned tissue slides with sodium citrate antigen retrieval solution for 15 min. Then, sectioned tissue slides were blocked by 5% BSA for 1 h, and subsequently incubated with primary antibodies against ITGα5 (1:200, ABclonal Technology) or p-AKT (1:400, Cell Signaling Technology) overnight. Alexa Fluor 594 or Alexa Fluor 488 secondary antibody was used to stain for 1 h, respectively. After PBS washing, sectioned tissue slides were stained with DAPI and viewed by CLSM.

2.6. Statistical analysis

Statistical analysis was conducted with SPSS-PC 22.0 Software (SPSS Inc., USA). The data were expressed as the mean ± standard deviation. Student's *t*-test was used to determine statistical differences in collagen and DNA content of tendon following decellularization treatment. The quantification of the WB assay was also analyzed by Student's *t*-test. As for the investigations of BLB roughness, contact angle, elastic modulus and HU value, the assays of cytotoxicity, cell proliferation, ALP activity, OCN content and the fold change of mRNA, as well as the analysis of BV/TV and bone density from micro-CT, one way ANOVA followed by Tukey test was used to determine statistical differences among groups. For all analyses, the level of significance was set as $p < 0.05$.

3. Results

3.1. Fabrication and hierarchical characterization of BCM

To guarantee engineered BCM was built by nondenatured collagen and tendon derived cells has been removed to the greatest extent. Decellularized tendon was first tested. As depicted from the immunofluorescence staining images (Fig. 1A), well-aligned organization of tendon was completely preserved following decellularization treatment. Meanwhile, the bundle structure of tendon was also retained (Fig. 1B). The collagen content was not considerably reduced after decellularization (Fig. 1C), certifying that subsequently constructed BCMs were primarily composed of collagen. In contrast, the DAPI signal staining nucleus was almost absent in decellularized tendon. The DNA content significantly decreased from 230.7 ± 17.3 ng/mg to 14.0 ± 1.4 ng/mg (Fig. 1D), illustrating that potential immunogenicity of subsequent constructs has been efficiently eliminated. Furthermore, the extracted culture media from decellularized tendon exerted no adverse effect on L929 cells at 1 d and 2 d in comparison with the control group (Fig. 1E), verifying the complete removal of cytotoxic SDS and EDTA.

The hierarchical architecture of BCM was investigated (Fig. 1F). The characteristic periodic cross-band of collagen fibril can be clearly found in the SEM image of BCM, revealing that BCM was built by collagen fibrils. The cross-section of SEM image presented the densely-packed multilamellar structures. The thickness of each collagen sheet was around 10 μm, which was extremely close to that of bone lamella in human. The collagen sheets were not oriented in the same direction and a periodic rotation pattern can be detected. There was a strong similarity between this multi-sheet structure and the collagen hierarchy of lamellar bone. To further examine the periodic distribution of sheet orientation in detail, the ortho-mode images of LSCM profilometer were displayed (Fig. 1F(d)). The colored layer referred to collagen sheet of which the fibril orientation was parallel to the plane. It emerged at periodic intervals. Colored layers (right insets) appeared 10 times along cross-section of BCM. Our BCMs contained 20 sheets and the occurrence frequency of collagen sheet with the same fibril orientation was in accordance with the theoretical value, suggesting that the orientation of stacked collagen sheets was accurately controlled during BCM construction. CD and DSC were employed to evaluate whether collagen in BCM was denatured. In the CD spectrum (Fig. 1G), gelatin, the denatured form of collagen, only revealed a single negative peak of lower

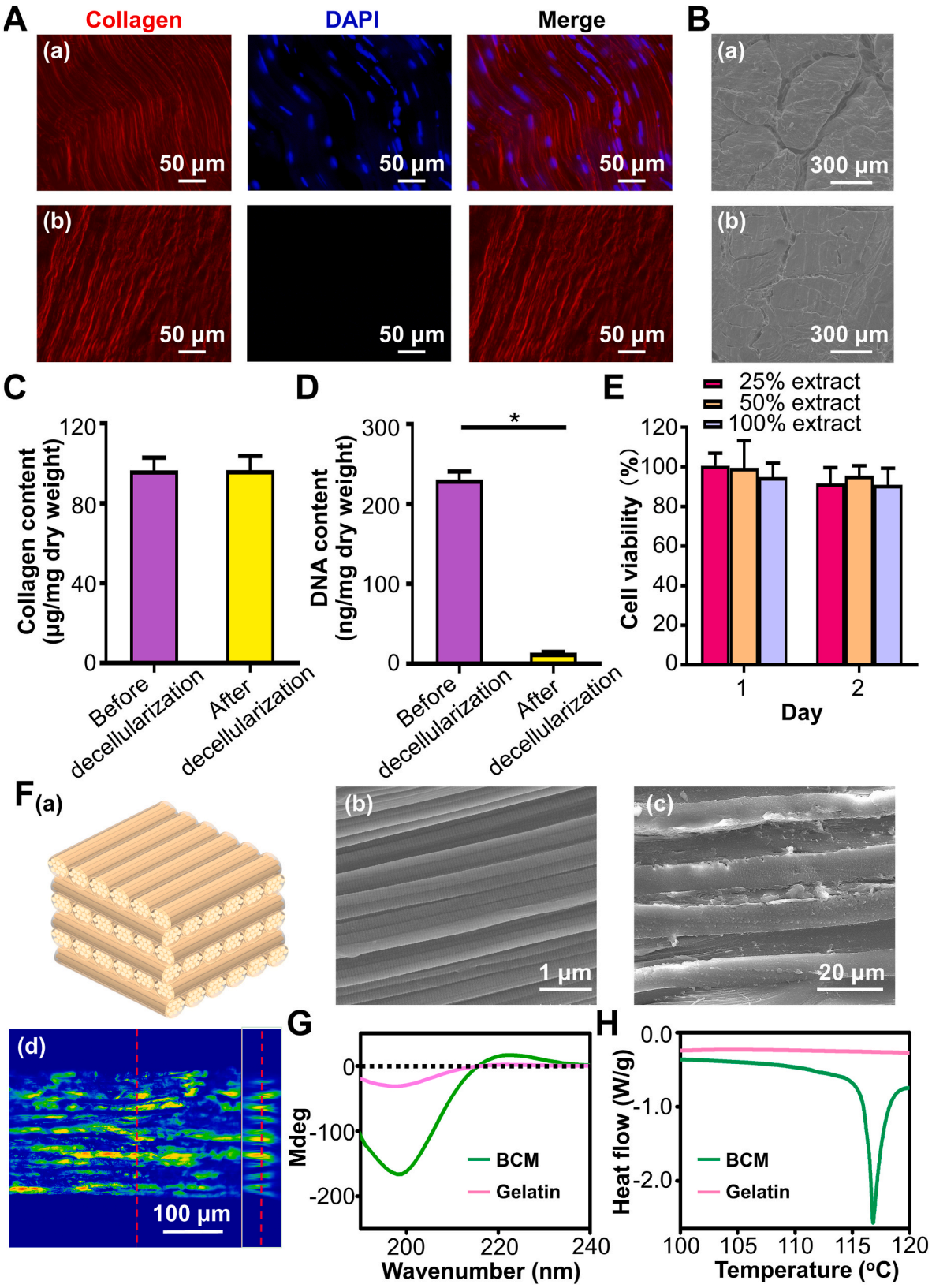

Fig. 1. The characterization of decellularized tendon and constructed BCM through bioskiving. (A) The immunofluorescent staining of collagen and DAPI of tendon before (a) and after (b) decellularization. (B) The cross-section SEM images of tendon before (a) and after (b) decellularization. (C) Collagen content and (D) DNA content of tendon before and after decellularization. (E) The different concentrations of extracted culture media from decellularized tendon on the viability of L929 cells. The asterisk on top of the bar indicated a statistically significant difference between groups ($p < 0.05$). (F) Hierarchical characterization of BCM. (a) Schematic illustrating the hierarchy of BCM stacked at 90°, (b) SEM image of BCM surface, (c) SEM image and (d) LSCM profilometer image of BCM from the view of cross-section. (G) CD and (H) DSC spectra of BCM and gelatin.

molar ellipticity, which was associated with random conformation of α-chains in gelatin [43]. On the contrary, BCM exhibited the typical sinusoidal spectra of natural collagen. Additionally, BCM exhibited an endothermic peak around 117 °C in the DSC spectrum (Fig. 1H), evidencing that the triple helix of collagen denatured to the random coil during heating process. Conversely, no endothermic peak was detected in the gelatin. The results of CD and DSC suggested that tendon decellularization and bioskiving fabrication process did not denature collagen.

3.2. Fabrication and physicochemical characterization of BLB

Visually, BCM appeared to be relatively transparent with an apparent crisscrossing texture (Fig. 2A). With the mineralization progressed, the constructs became increasingly opaque. Meanwhile, Alizarin red staining revealed that the constructs reddened following mineralization. The sequence of colors was BLB12d > BLB9d > BLB6d > BCM from deep to light. TEM images showed the nano-hierarchy of construct (Fig. 2B). BCM exhibited the typical staggered nanostructure of collagen fibril. As for BLB6d, a small amount of minerals was detected inside fibril. From the edge-on view of BLB9d, numerous nanoneedle-shaped minerals were manifested along the fibril axis. From the face-on view of BLB9d (Fig. S2A), plenty of crystals were periodically deposited in fibril. The nanostructure of collagen fibril in BLB9d was highly comparable with that of natural bone. However, as mineralization reached 12 d, the structure of mineralized collagen fibril was intangibly found, and considerable amounts of crystals were randomly attached to the surface of fibril, which impaired the hierarchical biomimicry of nanostructure. SEM images showed the micro-hierarchy of construct surface (Fig. 2C), BCM was featured by the highly-aligned architecture with striated nanostructure. As mineralization progressed from 6 d to 12 d, minerals gradually deposited. Of note, the unidirectional pattern can be distinctly detected. Nevertheless, massive bulk minerals were disorderly arranged on the surface of BLB12d, and the parallel pattern vanished accordingly. Analogously, the surface of BCM, BLB6d and BLB9d depicted the clearly parallel structure in LSCM profilometer images (Fig. 2D). BLB12d was characterized instead by the irregular surface. There was no significant difference in surface roughness among BCM, BLB6d and BLB9d (Fig. 2E). In contrast, the surface of BLB12d became prominently coarser.

As mineralization proceeded, the hydrophilicity of BLB was progressively enhanced (Fig. 2F). No dramatic difference regarding water contact angle was detected between BLB9d and BLB12d. The elasticity modulus of BLB9d (10.05 ± 1.17 GPa) was comparable with BLB12d (11.62 ± 3.81 GPa), which was significantly higher than that of BCM (1.03 ± 0.29 GPa) and BLB6d (3.48 ± 0.51 GPa) (Fig. 2G). XRD spectra demonstrated a hump around 20°-25° in BCM (Fig. 2H). The mineral crystals obtained on the surface and inside BLB were primarily the same. Only a weak peak around 32.2° was found in BLB6d. In comparison with standard XRD pattern of HA (JCPDS file number 9-0432), The distinctive peaks at 25.8° and 28.9° in the spectra of BLB9d and BLB12d were well fitted to the diffraction of (002) and (210) from standard HA. The broad peak around 32.2° was composed of overlapping peaks from (211), (112) and (300) plane of HA. Therefore, the crystals in BLB9d and BLB12d were HA. The broaden peaks in BLBs revealed the low crystallinity of HA. Since HA in natural bone was the biological form containing carbonate, ATR-FTIR was conducted to further evaluate whether the crystal in BLB could mimic the biological HA. As shown in Fig. S2B, the characteristic peaks of collagen (Amide I, Amide II, Amide III), HA (ν_1PO_4, ν_3PO_4) and ν_2CO_3 can be distinctly detected in BLB6d, BLB9d and BLB12d, illustrating that HA deposited in collagen fibril of BLBs resembled the biologically carbonate-containing HA of natural bone tissue.

Moreover, TGA was conducted to quantify HA content of BLB (Fig. 2I). No inorganics was found in BCM after heating to 700 °C, Accordingly, the inorganics primarily accounted for the remaining weight of BLB constructs when heated to 700 °C. The inorganic mass was 16.3%, 45.3% and 57.9% in BLB6d, BLB9d and BLB12d, respectively. Of note, the remaining mass in BLB6d, BLB9d and BLB12d slightly decreased to 15.7%, 44.8% and 55.0% after heating to 800 °C, respectively. The weight loss from 700 °C to 800 °C was related with the decomposition of carbonates in HA [47]. This weight loss percentage ranged from 1.1% to 5.0%, which was in accordance with the range for carbonates in natural bone mineral [48]. In addition, to verify that the effective mineralization of constructs, XPS was conducted (Fig. S2C). In comparison with the spectrum of BCM, the peaks of Ca2p, Ca2s, P2p and P2s can be found in BLBs, confirming that densely-packed collagen matrix fabricated by bioskving can be mineralized via ACP. The intensity of Ca2p, Ca2s, P2p and P2s in BLB9d and BLB12d was remarkably higher than that in BLB6d, which validated the results of XRD and TGA.

Cross-sectional SEM image of BLBs were presented (Fig. 3A) to investigate the internal hierarchical structure of BLBs. All BLBs exhibited densely-packed multilamellar architectures. Compared with BLB9d, a small number of irregular minerals can be found in small gap and fissure between lamellae of BLB12d. Beyond this, there was no dramatically difference in hierarchical architecture between BLB9d and BLB12d. To investigate the minerals distribution inside BLBs, elemental surface mapping of EDS was performed across the cross-section of constructs. BCM contained abundant C and O elements. Conversely, Ca and P elements were barely detected. BLB6d contains small amounts of Ca and P elements. Most Ca and P element distributed in the surface layer. As for BLB9d, abundant Ca and P element were deposited throughout entire cross-section. Even in the innermost regions of BLB9d, a large number of Ca and P can be detected, which evidenced the effective mineralizaiton of internal region. As for BLB12d, the amount of Ca and P element located in the internal region was not significantly augmented compared with those in BLB9d. However, Ca and P element located in the surface region of BLB12d continued to increase. BLBs were extremely dried during SEM sample preparation, to further assess the internal hierarchy under the physiological condition, BLBs in moist state were scanned by micro-CT (Fig. 3B). BCM, BLB6d, BLB9d and BLB12d remained compact multilamellar architecture under moist condition. Several fissures and pores introduced during manual stacking can be found inside constructs, which were considered as the auxiliary pathway for ACP to enter and mineralize constructs. The mineral distribution throughout constructs was also evaluate. Both surface region and internal region of BCM were radiolucent. There was no significant difference in HU value between surface region and internal region of BCM. Although surface region of BLB6d was slightly radiopaque, no statistical difference in HU value can be found between surface region and internal region. As for BLB9d, the overwhelming majority of constructs became radiopaque and HU value was dramatically increased compared with BLB6d. Meanwhile, HU value in surface region of BLB9d was significantly higher than internal region. Similarly, the surface region of BLB12d was more radiopaque than internal region. Interestingly, although HU value in surface region of BLB12d was significantly increased than that of BLB9d, HU value in internal region of BLB12d was comparable with that of BLB9d. Taken together, BLB mineralized 9 days could best mimic the full-scale hierarchy of lamellar bone.

3.3. In vitro osteogenic assay of BLB

After elucidating the influence of mineralization time on hierarchical biomimicry of constructs, the relationship between hierarchical mimicry and osteogenic bioactivity was further explored. The live/dead cell fluorescent staining of BMSCs (Fig. 4A) revealed that the vast majority of cells cultivated on BCM, BLB6d, BLB9d and BLB12d were viable (green fluorescence), suggesting that all constructs exhibited the satisfactory cytocompatibility. As the culturing time extended, the BMSCs density increased accordingly. Meanwhile, BMSCs were arranged in an oriented pattern on BCM, BLB6d and BLB9d. On the contrary, BMSCs were randomly grown on BLB12d. The immunofluorescence images staining

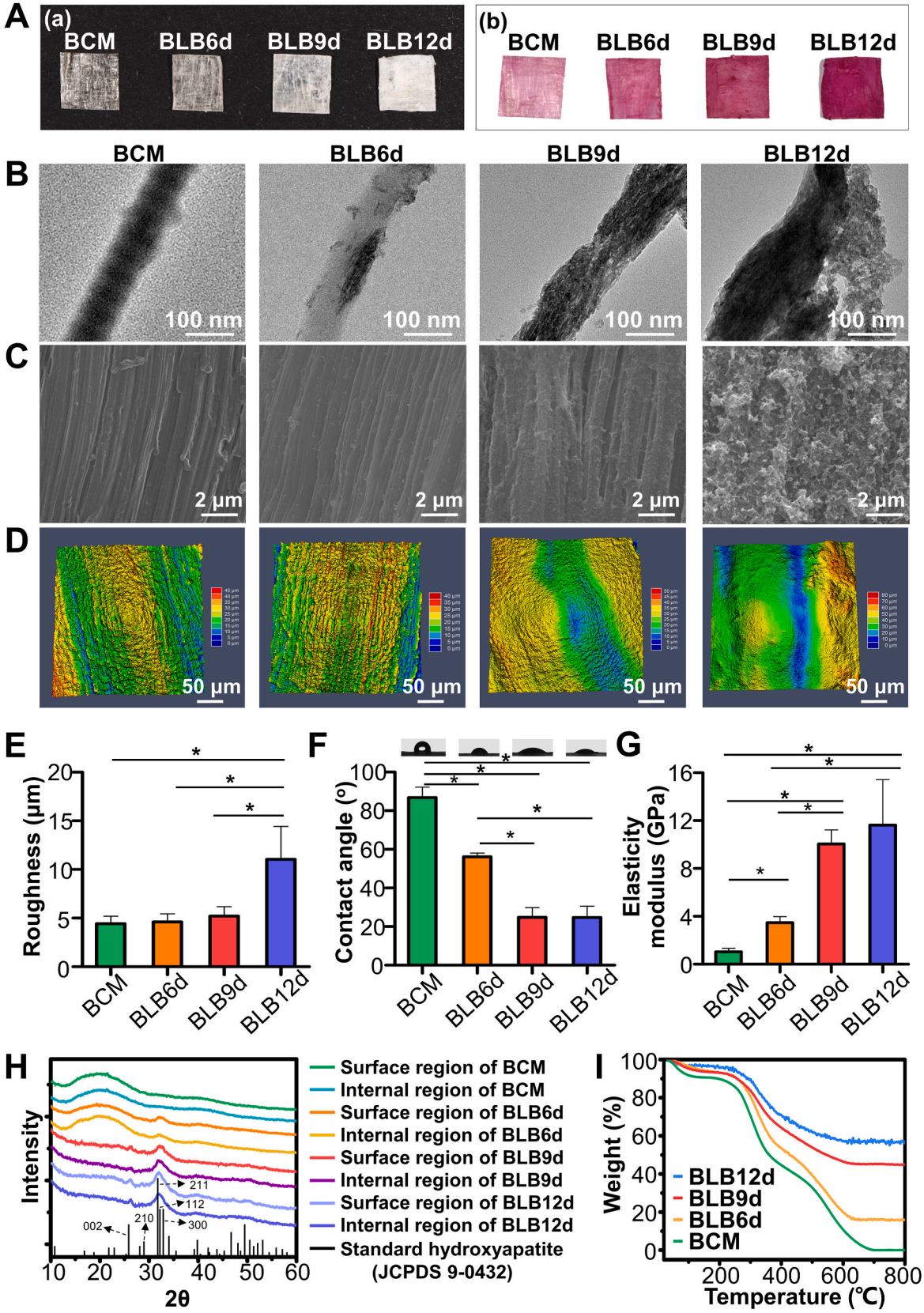

Fig. 2. Physicochemical characterization of BLBs mineralized at different times. (A) Photographs of BLBs stained (a) without and (b) with Alizarin Red S. (B) TEM images of BLBs. (C) SEM images and (D) LSCM profilometer images of BLB surfaces. (E) Surface roughness, (F) water contact angle, (G) elasticity modulus, (H) XRD spectra of surface and internal region of BLBs, (I) TGA results of BLBs. The asterisk on top of the bar indicated a statistically significant difference between groups ($p < 0.05$).

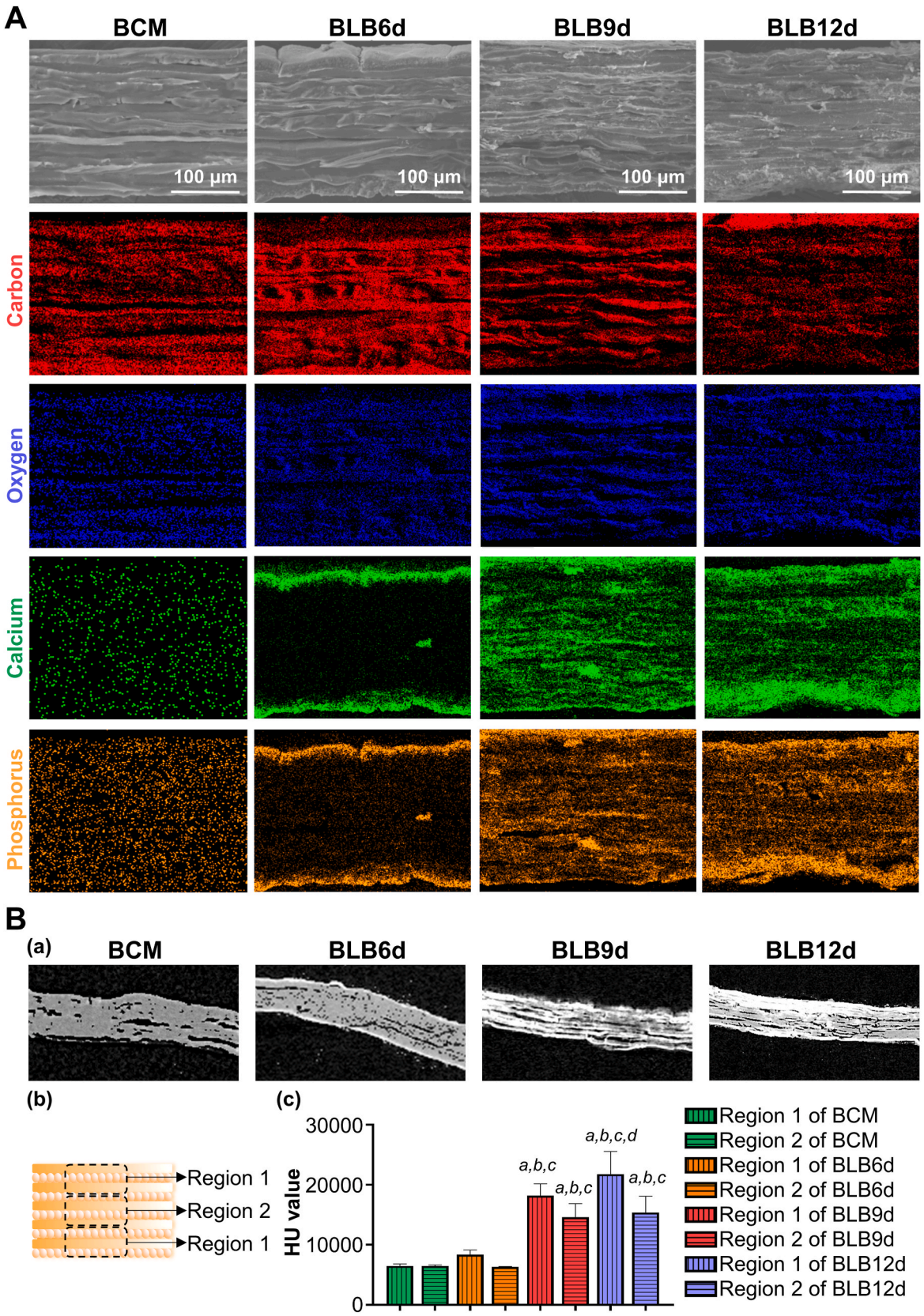

Fig. 3. Hierarchical characterization and composition analysis of BLBs mineralized at various times. (A) The SEM images and elemental mapping of EDS throughout the cross-section of BLBs. (B) (a) The micro-CT image of cross-section of BLBs. (b) Schematic diagram illustrating selected region of construct measuring HU value. Region 1 indicated the surface one-third region of construct. Region 2 indicated the internal third region of construct. (c) HU value of different region of construct. The statistically significant difference p was set as 0.05. *a* indicated a statistically significant difference between region 1 and 2 in the same construct. *b* indicated that there was a statistically significant difference in the same region compared with BCM. *c* indicated that there was a statistically significant difference in the same region compared with BLB6d. *d* indicated that there was a statistically significant difference in the same region compared with BLB9d.

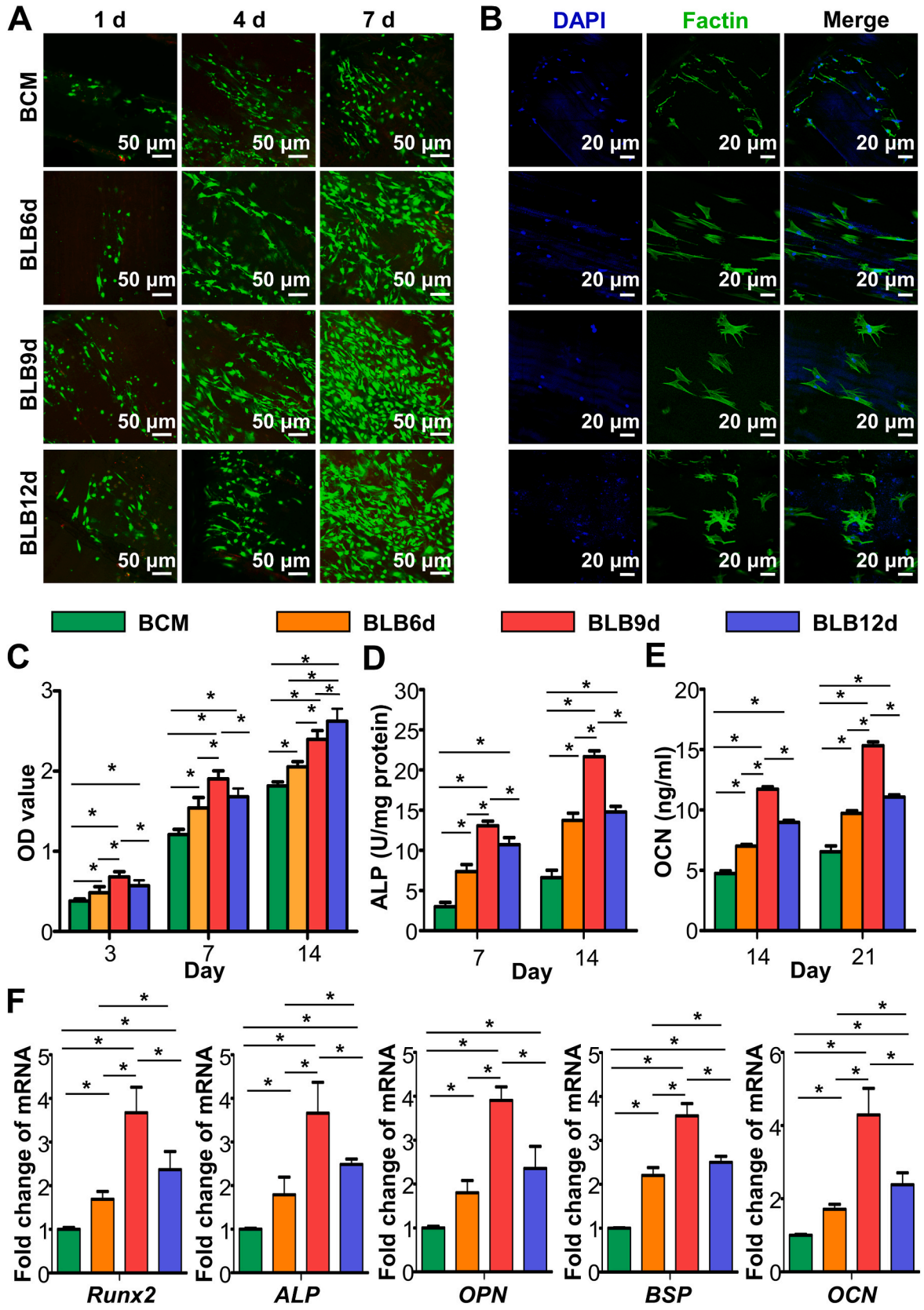

Fig. 4. In vitro osteogenic assay of BLBs mineralized at different times. (A) The representative live/dead images of BMSCs cultured on BLBs at day 1, 4 and 7. (B) F-actin cytoskeleton and nuclei of BMSCs cultured on BLBs at day 1. (C) The CCK-8 results of BMSCs proliferation at day 3, 7 and 14. (D) ALP activity of BMSCs at day 7 and 14. (E) OCN production of BMSCs at day 14 and 21. (F) Osteogenic gene expression results of BMSCs cultured on BLBs at day 14. The asterisk on top of the bar indicated a statistically significant difference between groups ($p < 0.05$).

of cytoskeleton were shown in Fig. 4B. After seeding 24 h, BMSCs spread on BCM exhibited the polarized outline with thin actin fibrils and sparse cellular processes. The cells BMSCs spread on BLB6d showed extended cellular processes with thicker actin fibrils. It is also noteworthy that BLB9d and BLB12d have more branched filopodia. However, the filopodia in BLB9d were in oriented arrangement, whereas the filopodia in BLB12d were irregularly arranged. Fig. 4C presented the CCK-8 results of BMSCs. OD value of BLB9d was statistically higher than other constructs at day 3 and 7, indicating that BLB9d was beneficial to proliferation. At day 14, there was no significant difference existed in OD value between BLB9d and BLB12d, suggesting that cells grown on BLB9d reached confluence and were in the process of differentiation.

In terms of ALP (an early marker of osteoblastic differentiation) activity and OCN (a late marker of osteoblastic differentiation) content, BLBs were effective in improving osteogenic differentiation of BMSCs in comparison with BCM at predetermined time points (Fig. 4D and E). Thereinto, BLB9d exhibited superior performance. To qualitatively confirm the osteogenic ability of BLB9d, real-time PCR was conducted at day 14 (Fig. 4F). The relative mRNA expression levels of osteogenic differentiation related genes, *Runx2, ALP, OPN, BSP and OCN*, were significantly upregulated in BLB9d compared with other constructs.

Based on the result of physicochemical characterization and osteogenic bioactivity, BLB9d was considered to present optimal hierarchical mimicry of lamellar bone and provide favorable microenvironment for BMSCs osteogenesis. Therefore, BLB9d was selected and utilized in the following animal study and bioinformatic analysis.

3.4. Bone regeneration behaviour of BLB in vivo

Based on the excellent osteogenesis of BLB9d in vitro, we further explored its performance to repair bone defect. The 3D reconstruction images of rat skull defects after 12-week postimplantation were shown in Fig. 5A. In the superficial view, no significant new bone formation was found in blank group, indicating that rats did not have self-regeneration ability to repair critical-sized bone defect. Even though a minor amount of bone was formed in BCM group, the new bone formation area was less than half of the defect area. The skull defect in BLB9d group was almost entirely healed by newly formed bone tissue. Similarly, the skull defect was totally occupied by bone tissue in autograft group. In the coronal and sagittal planes, blank group showed almost no newborn bone, while BCM group demonstrated limited newly formed bone at the defect margin. As for the BLB9d group, regenerative bone tissue has effectively bridged the bony defect. Relatively continuous and intact bone was found in autograft group. BV/TV and bone density of newly formed bone in BLB9d group were significantly higher than those of blank and BCM group (Fig. 5B and C).

HE staining images (Fig. 5D) showed that the skull defect in blank group was nearly entirely filled by the fibrous connective tissues rich in blood vessels and only extremely limited bone was found around defect edge. With regard to the BCM group, some regenerative bone can be seen at the defect margin and the defect was still principally repaired by the fibrous connective tissue. As for BLB9d group, the defect was almost completely restored by the densely packed bone, despite that the maturity of regenerated bone tissue was slightly inferior to that in autograft group (Fig. 5E). The immunofluorescent staining showed that neither blank nor BCM group manifested high levels of OCN (Fig. S3), confirming that defect was mainly restored by fibrous connective tissues rather than bone. By contrast, the majority of cells in BLB9d and autograft group were OCN-positive cells, indicating that BLB9d can boost bone formation during healing.

3.5. Activation of ITGα5-PI3K/AKT signaling pathway by BLB9d for enhanced BMSCs osteogenesis

To investigate the underlying molecular mechanisms through which BLB9d promoted osteogenesis of BMSCs, we conducted bioinformatic analysis and investigated the profile of functional genes of BMSCs in BCM and BLB9d group via RNA sequencing. The volcano plot displayed a total of 179 differentially expressed genes ($|\mathrm{Log_2\ FC}|>1.0$, $p < 0.05$), indicating different expression patterns during osteogenesis (Fig. 6A). The entire heatmap also showed different gene profiles between BCM and BLB9d group (Fig. S5). KEGG enrichment analysis indicated that PI3K/AKT signaling pathway was ranked first within differentially expressed genes (Fig. 6B). GO term analysis (cellular component) showed that the differentially expressed genes were predominantly located in the integrin complex (Fig. 6C). Cell-cell adhesion mediated by integrin was the major biological process according to Go enrichment analysis (Fig. S3B). Go enrichment analysis further demonstrated that growth factor binding and cell adhesion molecule binding were the main molecular function of the differentially expressed genes (Fig. S4C). Thus, among the top twenty enriched signaling pathways, we focused on PI3K/AKT signaling pathway which was strongly associated to the upregulated region for BLB9d group than BCM group according to GSEA enrichment (Fig. 6D). The cluster heatmap involving PI3K/AKT signaling pathway demonstrated that the upregulated key effector genes in the BLB9d group included ITGα4 and ITGα5 compared with BCM group (Fig. 6E). Based on previous studies which indicate that ITGα5 offers topological and mechanical cues to promote osteogenic differentiation of mesenchymal stem cells [49,50], we further verified that the expression of ITGα5 and p-AKT in the BLB9d group increased up to 4.01-fold and 3.09-fold compared with BCM (Fig. 6F and G). Taken together, we concluded that BLB9d enhanced BMSCs osteogenesis by activating ITGα5-PI3K/AKT signaling pathway.

To further verify that BLB9d induced osteogenesis through activation of ITGα5-PI3K/AKT signaling pathway in vivo, the immunofluorescent staining of ITGα5 and p-AKT was conducted (Figs. S6 and 7). As for blank and BCM group, only extremely low level of ITGα5 and p-AKT were expressed. On the contrary, the newly generated tissue in BLB9d group had an increased level of ITGα5 and p-AKT expression. Both ITGα5 and p-AKT expression was comparable between BLB9d and autograft group, suggesting that activation of ITGα5-PI3K/AKT pathway was determinant to the osteogenic effect of BLB9d construct.

4. Discussion

Lamellar bone is the structural motif of mature bone. Simulating lamellar bone is the top priority in engineering biomimetic cortical and trabecular bone to fulfill the urgent clinical demand. In particular, its exquisite full-scale hierarchy endowed lamellar bone with multiple intrinsic and fascinating functions. Each hierarchical scale, from the basic component to the twisted plywood architecture, exerts an essential role. Promisingly, MFS is a well-established approach for constructing bone hierarchy. Two critical aspects, collagen matrix assembly and following mineralization, are involved in MFS. Of note, although mineralization is of vital importance to simulating micro- and nanostructure of bone, the mimicry of bone hierarchy is primarily determined by the framework of collagen matrix. Collagen matrix can be constructed via bottom-up strategy, assembling fibrils from the collagen molecular level, or top-down strategy, using collagen tissue ingeniously build by nature. So far, a substantial progress has been made in fabricating the collagen matrix of lamellar bone. For instance, it has been reported that collagen solution can be densified and assembled into the matrix with a hierarchical similarity to lamellar bone [51–53]. However, the orientation and alignment of collagen fibrils cannot perfectly mimic those of lamellar bone. The intrinsic reason for this inferior mimicry lies in the fact that in vitro self-assembly of collagen directed by bottom-up strategy fails to accurately resemble the complicated and precise in vivo assembly process. During bone formation, the organization of collagen fibrils is strictly controlled by the direction of cellular processes [54]. As the formation of lamellar bone is ongoing, numerous cells all extend processes in a parallel direction. Correspondingly, collagen proteins are secreted and assembled along the direction of

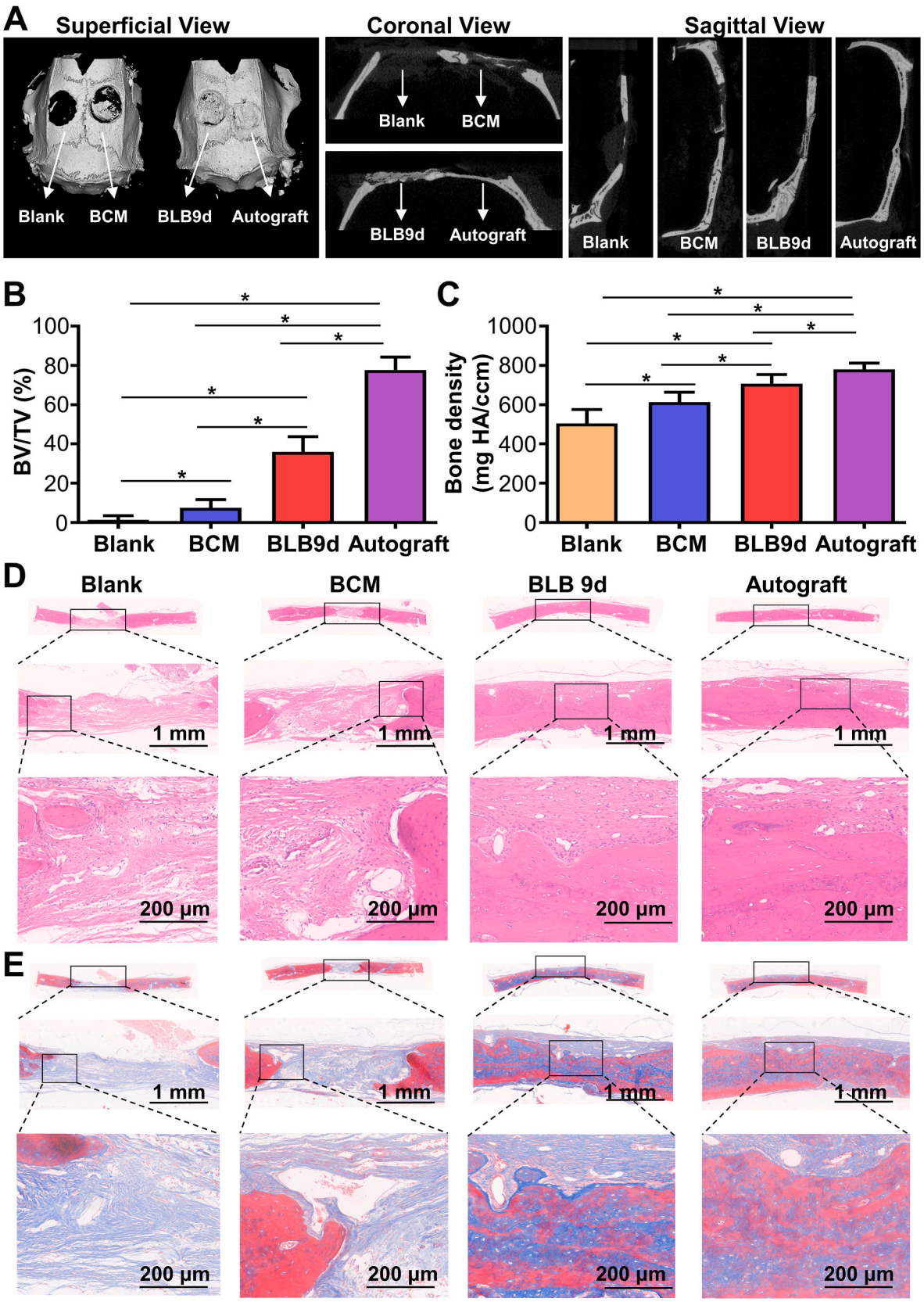

Fig. 5. Bone regeneration of BLB9d after implanted in critical-sized bone defect. (A) Micro-CT images of regenerated tissue after 12-week postimplantation. (B) BV/TV and (C) bone density of regenerated tissue. (D) HE and (E) Masson's trichrome staining images. The asterisk on top of the bar indicated a statistically significant difference between groups ($p < 0.05$).

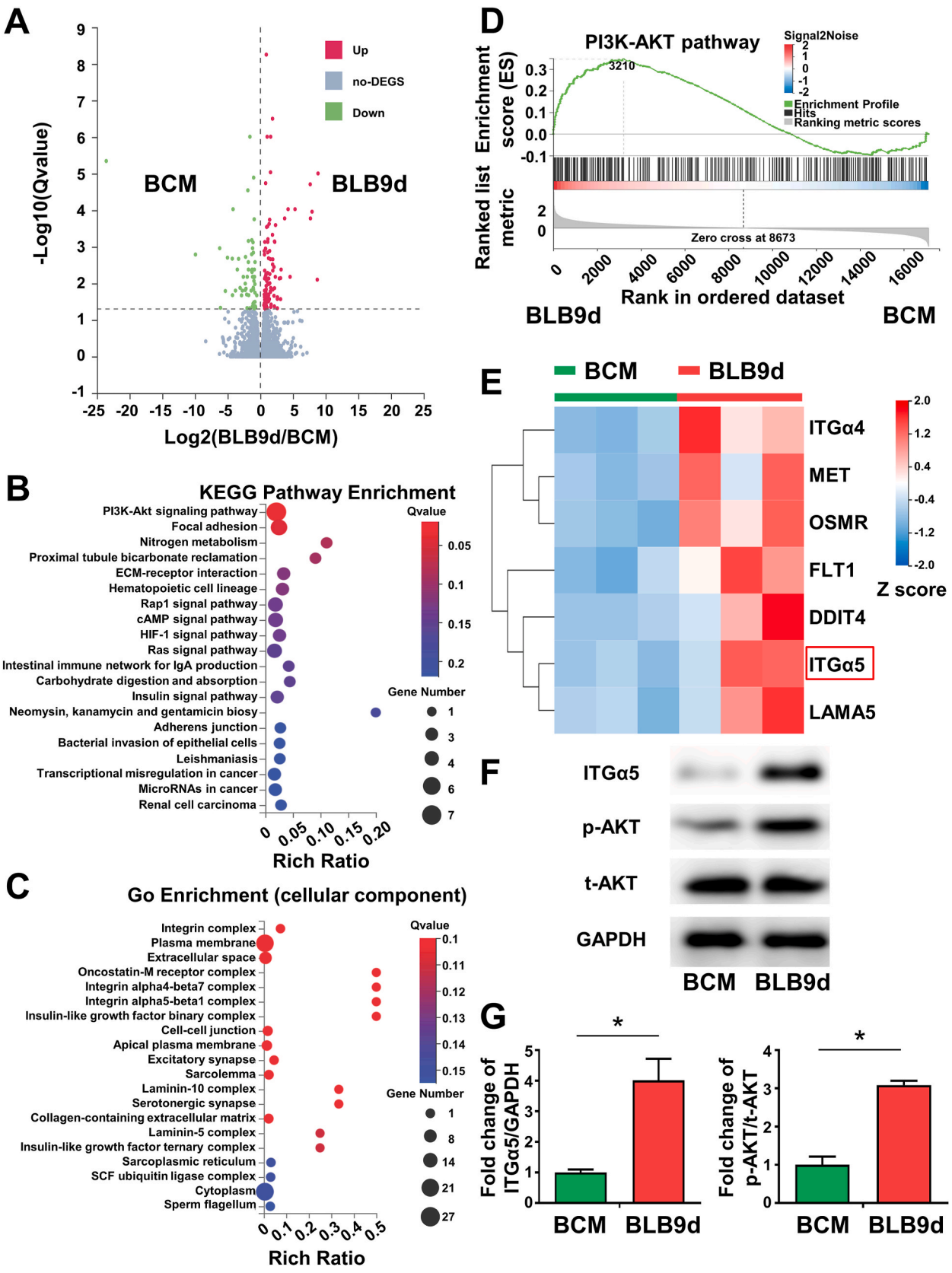

Fig. 6. Activation of ITGα5-PI3K/AKT pathway by BLB9d for BMSCs osteogenesis. (A) The volcano plot of differential expression of genes between BLB9d and BCM group: the up-regulated, unchanged genes, and down-regulated were doted in red, gray, and green, respectively. (B) The top twenty enriched signaling pathways following KEGG enrichment analysis for differential expressed genes. (C) GO enrichment analysis for differential expressed genes (cellular component). (D) GSEA enrichment plots of gene set involved in PI3K/AKT signaling pathway. (E) A cluster heatmap showed differentially expressed genes involved in PI3K/AKT signaling pathway ($|\text{Log}_2\ \text{FC}|>1$). (F) Representative western blotting images of ITGα5, p-AKT and t-AKT proteins. (G) Quantitative statistical analysis of fold change of ITGα5/GAPDH and p-AKT/t-AKT. The asterisk on top of the bar indicated a statistically significant difference between groups ($p < 0.05$).

process, thus forming the unidirectional pattern of collagen fibril. Afterwards, cellular processes rotate in a synchronous and periodical way before further producing parallel fibrils, resulting in altered fibril orientation between adjacent lamellae and eventually generating twisted plywood architecture.

This in vivo assembly process can be well imitated by bioskiving directed by top-down strategy. Decellularized tendon, formed by eliminating cell from native tendon, has attracted tremendous attention in serving as a prospective scaffold for tendon repair due to its ability to preserve structural and functional proteins [55]. The well-aligned architecture of decellularized tendon could provide an appropriate structural microenvironment and exemplary mechanical trait for differentiation of stem cells. Previous studies evidenced that decellularized tendon could efficiently guide the growth of tenocytes and induce the cellular integration throughout the depth of the scaffold [56]. In this study, we further extended the application of decellularized tendon to the construction of biomimetic bone, in which decellularized tendon was sectioned and stacked by bioskiving. As demonstrated in Fig. 1C, collagen content of tendon was not dramatically reduced after decellularization, which guaranteed that our constructs were built by collagen (level I). Meanwhile, CD (Fig. 1G) and DSC results (Fig. 1H) confirmed that collagen in BCM was not denatured. The quarter-staggered nanostructure (level II) and the array of collagen fibril (level III) remained intact (Fig. 1F). The mimicry of collagen unidirectional pattern (level IV) can be simply implemented via sectioning procedure, whose thickness can be rigorously restricted to mimic bundles of bone lamella (level V). The simulation of twisted plywood architecture (level VI) can be achieved via further stacking procedure (Fig. 1F). As demonstrated by SEM and LSCM profilometer of BCMs, the occurrence frequency of collagen sheet with the same orientation direction was in agreement with the theoretical value, evidencing that bioskiving was able to precisely control rotation angle between neighboring sheets.

In addition to the construction of collagen matrix, mineralization is another key aspect determining the hierarchical mimicry in the respect of micro- and nano-structure [57]. Unfortunately, the vast majority of studies focus on mineralizing loosely-packed collagen scaffold, in which ACP could easily penetrate into the spongy-like scaffold and mineralize collagen fibril. However, since the architecture of densely-arranged collagen matrix is totally different from that of spongy-like scaffold, whether ACP could infiltrate compact matrix and efficiently mineralize collagen fibril was rarely clarified in detail. Hence, in order to elucidate the influence of mineralization on the hierarchical mimicry of lamellar bone, physicochemical traits of BCM, BLB6d, BLB9d and BLB12d were systematically evaluated in this study.

As demonstrated by elemental mapping of EDS and micro-CT images (Fig. 3), ACP could penetrate surface region of BCM, enter deep region and implement the mineralization with time prolonging. As mineralization extended from 0 d to 9 d, mineralization of collagen fibril was progressively intensified (Fig. 2B and S2A). Correspondingly, nHA content, hydrophilicity and elastic modulus of BLBs were enhanced (Fig. 2F, G and I). Neither the surface roughness nor the parallel microstructure was affected (Fig. 2C, D and E). Hence, as mineralization proceeded from 0 d to 9 d, hierarchical mimicry of BLB enhanced. Interestingly, as mineralization reached 12 d, the inner architecture of BLB12d was not significantly altered. Compared with BLB9d, the minerals in internal region of BLB12d was not enhanced (Fig. 3A and B). However, the minerals in surface region of BLB12d was remarkably increased. Demonstrated by SEM (Fig. 2C), the surface was covered with massive irregular crystals at random. Moreover, the surface of BLB12d was considerably roughened and unidirectional pattern was virtually vanished (Fig. 2D and E). Although nHA content continued to increase (Fig. 2I), no significant changes were detected in elastic modulus (Fig. 2G). This result was presumed to be related with mechanical property of mineralized collagen, which was mainly originated from the intrafibrillar crystal rather than extrafibrillar crystal [25,58]. Therefore, as mineralization extended from 9 d to 12 d, hierarchical mimicry of BLB impaired. Taken together, mineralization time was shown to modulate hierarchical mimicry of lamellar bone in a bidirectional manner. The hierarchical mimicry performed the tendency of first rising then descending with incremental mineralization time.

The mechanism for this bidirectional modulation of hierarchical mimicry was speculated to be related with transition of mineralization from nonclassical crystallization to classical crystallization (Fig. 7). Initially, mineralization of BCM was dominated by nonclassical crystallization. The previous study demonstrated that polymer could only penetrate into turkey tendon at a depth of 100 μm. However, polymer-stabilized ACP was able to diffuse at least 200 μm into turkey tendon, evidencing that capillary force could drive polymer-stabilized ACP infiltrating into dense collagen scaffold [15]. The thickness of BCM was 200 μm. Hence, with the help of capillary force, carboxymethyl chitosan-stabilized ACP penetrated across the surface region of BCM and entered the internal region. Meanwhile, the fissures and pores inside BCM also served as the auxiliary pathway for ACP to enter internal region. Currently, various theories and model have been developed to elucidate the mineralization of collagen fibril, including electrostatic attraction, capillary force, size exclusion effect as well as the balance between osmotic equilibrium and electroneutrality [59,60]. It seemed reasonable to speculate that all these theories might occur simultaneously. Correspondingly, ACP entered collagen fibril through multiple forces and preferentially deposited inside the gap zones as well as overlap zones. Then, deposited ACP gradually and spontaneously transformed into nHA through nonclassical crystallization pathway. Since the nucleation and growth orientation of nHA was strictly confined by gap zones and overlap zones of collagen fibril, collagen fibrils played an irreplaceable role in serving as the template controlling HA during this stage. As the mineralization proceeding, ACP continue to penetrate inward and transformed into nHA. The hierarchically and orderly deposited nHA favored the enhancement of crystal content, hydrophilicity and elastic modulus of BLB. Meanwhile, attributed to the template effect of collagen fibrils, deposited nHA did not substantially alter the surface roughness and well-aligned microstructure for each lamella. Therefore, hierarchical mimicry of BLB enhanced as the mineralization proceeds. Due to the compact nature of BLB, once the nHA located in the surface region of BLB exceeded to a certain extent, it could block the pathway and prevent ACP from efficiently infiltrating inward. Consequently, the mineralization of collagen fibrils cannot proceed to enhance, especially for those located in the innermost region of BLB. More seriously, nHA located at the surface layer of BLB could act as the nucleation site to attract calcium and phosphate. The local supersaturation of calcium and phosphate leaded to the heterogeneous crystallization [61]. In turn, the newly formed crystals further blocked the infiltration pathway of ACP and concentrated more calcium and phosphate. Therefore, the mineralization mechanism was gradually transformed into the classical crystallization. As the crystals epitaxially grew from residual mineral located at the surface of BLB, collagen fibrils cannot continue to function as the template. Eventually, a large number of crystals were unevenly distributed on the surface of BLB, leading to an apparent increase of surface roughness as well as the disappearance of parallel microstructure and unique nanostructure. In consequence, hierarchical mimicry impaired as the mineralization proceeds. Based on this bidirectional regulation of mineralization time on hierarchical mimicry, BLB9d was selected as the optimal construct to mimic lamellar bone.

In order to mimic full-scale hierarchy of lamellar bone rather than only resembling partial hierarchy, e.g. structure of oriented lamellae or twisted plywood architecture, each hierarchical scale should be simulated. we have conducted series of characterization to investigate each scale of BLB9d. First and foremost, BLB9d was constructed based on MFS strategy, through which only collagen and HA can be contained in BLB9d. Demonstrated by the results of CD, DSC, XRD and ATR-FTIR (Fig. 1G, H, 2H and S2Bs), collagen protein was undenatured and HA

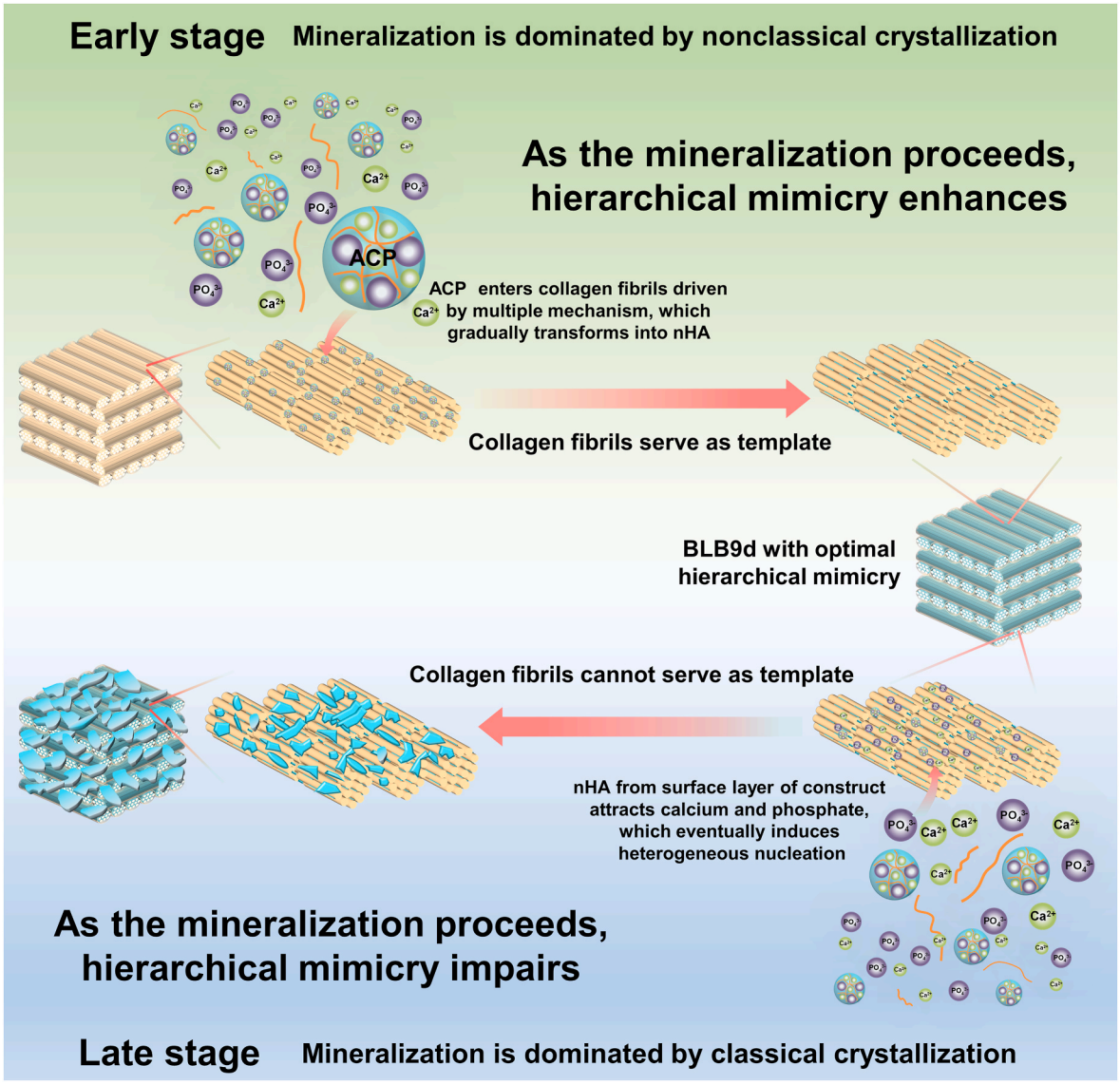

Fig. 7. The illustration of potential relationship between hierarchical mimicry of BLB and transformation of mineralization mechanism.

belonged to the poorly crystalline carbonated form, which were highly similar to the bone major components and achieved the simulation of level I. Since mineralized collagen fibril was essential building block of natural bone, the mimicry of its nano-hierarchy was of vital importance to the construction of biomimetic bone. Shown by TEM images of BLB9d (Fig. 2B and S2A), the typical view of edge-on and face-on projections of crystals in the mineralized collagen fibril can be clearly detected, indicating that HA preferentially deposited inside the gap zones and extended into the overlap zones of collagen fibril. The c-axis of HA is well aligned with the long axis of the collagen fibril. The nano-hierarchy of mineralized collagen fibril in BLB9d was identical with that in natural bone [1] (level II) as well as those in published papers [10]. The mimicry of its micro-hierarchy was another crucial issue to engineer lamellar bone. The unidirectional pattern of mineralized collagen fibril array (level III and IV) can be detected in BLB9d by SEM and LSCM profilometer (Fig. 2C and D), which was strongly reminiscent of the most classical array pattern in lamellar bone [1]. Furthermore, BLB9d exhibited the distinct architecture of bone lamella (level V) and the typical twisted plywood architecture (level VI). Currently, molecular crowding technique was the most mainstream approach to construct twisted plywood architecture [52]. However, the matrix prepared by molecular crowding technique was not homogeneous and only partial region of matrix contained twisted plywood architecture [51]. Moreover, the collagen fibril in each lamella was not highly aligned and the orientation between adjacent lamellae was random. The hierarchical mimicry of twisted plywood architecture was not optimum. By contrast, BLB9d possessed a well-defined and compact multilamellar architecture, of which lamellae thickness was close to human dimension and the periodic rotation pattern among lamellae was precisely controlled. The twisted plywood architecture of BLB9d shared strong similarity with that of human lamellar bone [62]. The constructs prepared by bioskiving and mineralization in our study was homogeneous and rotation degree between adjacent lamellae was manually controllable, which could act as a fundamental research model for further exploring the structure-function relationship of lamellar bone in depth. Based on the above investigations, although there were still some shortcomings existed in our hierarchical mimicry, we have preliminarily realized the full-scale hierarchy simulation of lamellar bone (Fig. 8).

The mechanical strength was the critical property for engineer bone. Based on the concept to completely mimic the full-scale hierarchy of lamellar bone, the elastic modulus of our construct (GPa) was is much higher than those simulating partial hierarchy (ranging from a few to several tens MPa) [4,63]. Although the elastic modulus of BLB9d was still slightly less than that of cortical bone (ranging from 14.53 GPa to

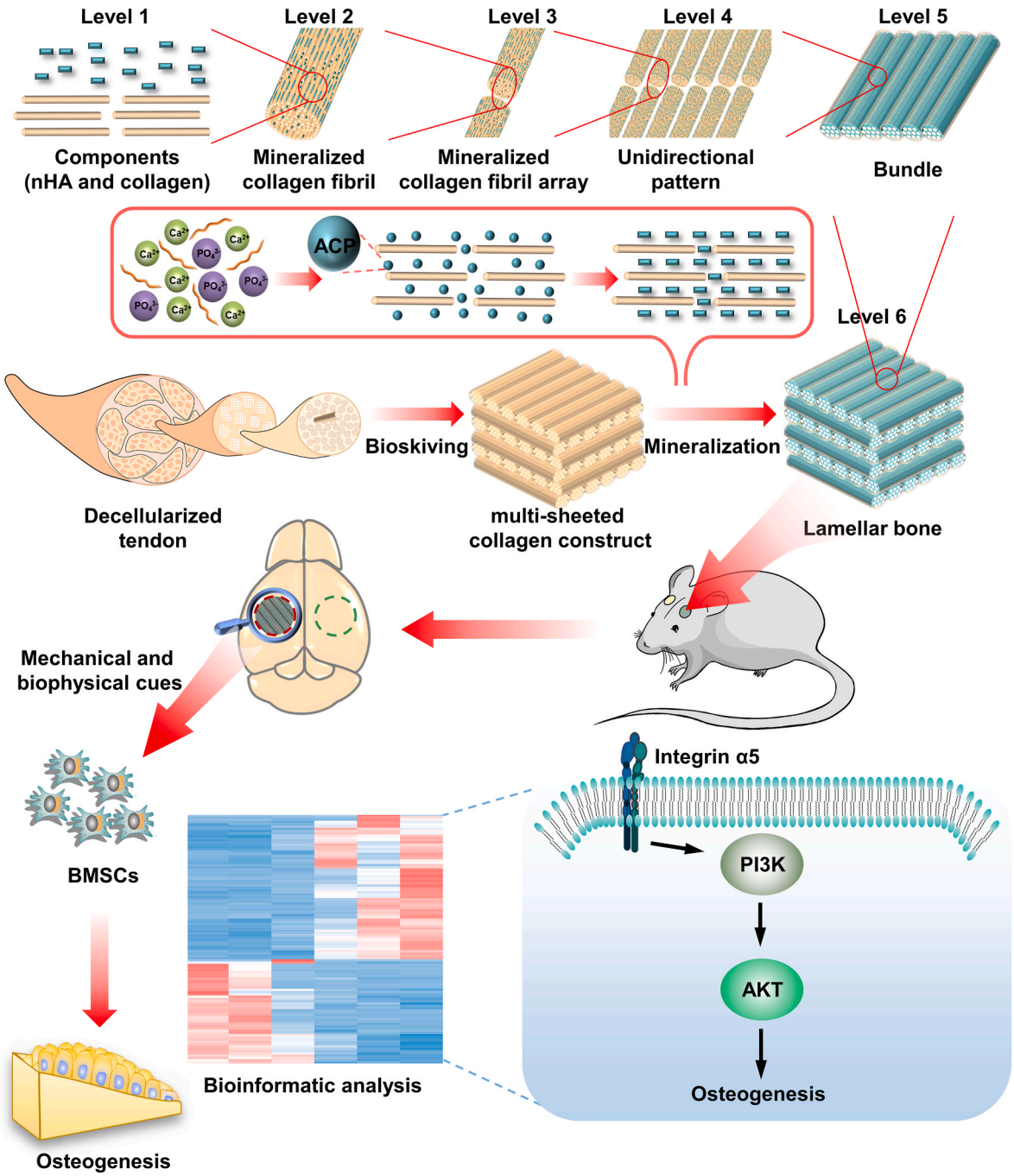

Fig. 8. Schematic illustrating engineered BLB mimicking full-scale hierarchy of lamella bone and promoting osteogenesis via activating ITGα5-PI3K/AKT signaling pathway.

19.47 GPa) [64], its mechanical property was of the same order of magnitude as cortical bone. Moreover, it manifested more superior mechanical performance than engineered lamellar bone prepared by molecular crowding technique (ranging from 4.2 GPa to 8.4 GPa) [51].

Functional biomimicry is closely associated with hierarchical biomimicry. Since BMSCs were seeded on the surface of BLB, biomimetic simulation of surface hierarchy exerts a profound influence on cell behavior. In accordance with the alteration of hierarchical biomimicry, the osteogenic bioactivities of BLB underwent a trend of first strengthening and then weakening. The present study showed that BLB9d has a superior performance in promoting proliferation, cytoskeleton reorganization and osteogenic differentiation of BMSCs (Fig. 4), which was supposed to be intimately associated with mimicry of hierarchy. BLB9d could provide both mechanical cue (high elastic modulus) and biophysical cue (micro- and nano-topology) to induce osteogenesis. Hereinto, BLB9d and BLB6d had a similar surface roughness and parallel microstructure. However, the elastic modulus of BLB9d was remarkably increased. As evidenced [14,65], the elastic modulus of material was of vital importance to the osteogenic differentiation. The high elastic modulus directed the differentiation of stem cells towards the osteogenic lineage. Hence, in comparison with BLB6d, BLB9d remarkably enhanced osteogenesis through providing mechanical cue. As for BLB12d, although its elastic modulus was comparable to that of BLB9d, both the unidirectional micro-pattern of lamellae and unique nano-topology of mineralized collagen fibrils vanished owing to the excessive and uncontrolled mineralization. The micro- and nano-topology of mineralized

tissue could exert the crucial role in modulating the fate of stem cell [24,26]. Thereby, the reason the osteogenic capability of BLB9d was superior than that of BLB12d lied in that BLB9d offered the favorable biophysical cue for cells. Bioinformatic analysis further demonstrated that the potent osteogenesis of BLB9d was tightly related with the activation of ITGα5-PI3K/AKT signaling pathway (Fig. 6). Previous study demonstrated that osteogenic differentiation of BMSCs grown on substrate with high elastic modulus was highly correlated with the activation of PI3K/AKT. Further investigation revealed that ITGα5 was involved in the enhancement of osteogenic outcome, in which matrix stiffness triggered mechanosensitive PI3K/AKT signaling cascade [66]. Meanwhile, relevant research indicated that ITG-PI3K/AKT signaling axis played a crucial role in hierarchical topography motivating cell adhesion, proliferation and osteogenic differentiation [67]. Therefore, the activation of ITGα5-PI3K/AKT signaling pathway in BLB9d was closely related with synergistically providing both mechanical and biophysical cues for BMSCs.

The objective of this study was to engineer biomimetic construct mimicking the full-scale hierarchy of lamellar bone. Although lamellar bone is the fundamental structure to construct cortical bone, the pure form of lamellar bone, known as circumferential lamellar bone, mainly locates in the outermost and innermost region of cortical bone, which only accounts for a very small proportion of cortical bone. The overwhelming majority of cortical bone is made up of by osteons. The hierarchy of osteon is more complicated than that of lamellar bone. Therefore, in order to guarantee our biomimetic construct match the hierarchical architecture of bone defect, our study did not select the commonly-used cortical bone defect model like femur defect. As reported [68], bone marrow, mainly formed by spongy bone, is relatively deficient in cranial bone. More importantly, the cranial bone is primarily composed by lamellar bone and there is no osteon in rat calvaria [69]. Meanwhile, since plenty of studies use the histologic formation of lamellar bone as a critical parameter to evaluate the osteogenesis effect of bone graft [70,71], which also indicates that lamellar bone is the main structure in rat calvaria. Hence, rat cranial bone defect model was used to evaluate the osteogenic performance of biomimetic lamellar bone in our study. The animal study verified that BLB9d possessed an outstanding performance in terms of repairing critical size of bone defect. The immunofluorescent staining of tissue also confirmed that the excellent osteogenic outcome of BLB9d was strongly linked with the activation of PI3K/AKT signaling pathway (Figs. S6 and 7). It is noteworthy that the maturity of regenerated bone tissue in BLB9d group was slightly inferior to that of autograft group (Fig. 5). This could be explained by the fact that autogenous bone is rich in osteogenic cells and cytokine besides hierarchical architecture. In this study, we have preliminarily realized the full-scale hierarchy simulation of lamellar bone. However, some vital non-collagen proteins and cytokines, e.g. osteonectin, osteonectin and bone morphogenetic protein, of which dose was extremely low in bone tissue but exerted the crucial role during bone regeneration, were not included in our construct. In addition, the dilemma of efficiently loading osteogenic cells into internal lamellae of compact construct was not explored. The gap in bone regeneration between our constructs and autograft is expected to be narrowed by efficiently doping cytokines and loading cells into the BLB in our next experiment.

In the present study, the rotation degree among bone lamellae in constructed BLB was set as 90^{o} according to the typical twisted plywood model of lamellar bone described by Gebhardt [21]. However, the exact rotation degree among bone lamellae in vivo is not defined to date [1], and the relationship between hierarchy of rotation degree and property remains to be elucidated. Through bioskiving and mineralization, BLBs with various rotation degree can also be constructed (Figs. S8 and S9), which could provide an essential research model for clarifying the structure-function relationship of lamellar bone in depth and pave a way for constructing various type of BLBs to meet clinical demand in the future.

5. Conclusion

In this study, the engineered lamellar bone resembling its full-scale hierarchy was fabricated by integration of bioskiving and mineralization strategies. Due to the compact nature of construct, hierarchical mimicry of BLB is performed in a bidirectional manner with prolongation of mineralization, which is supposed to be related with transformation of mineralization mechanism from nonclassical crystallization towards classical crystallization. Through tuning the mineralization time, the full-thickness mineralization of constructs can be realized to precisely resemble each hierarchical scale, leading to the favorable mechanical and biophysical properties. Correspondingly, osteogenic bioactivity was realized to a great extent through activating ITGα5-PI3K/AKT signaling pathway. More sophisticated hierarchy of compacted mineralized tissue is supposed to be constructed via this bioinspired strategy in the future.

Ethics approval and consent to participate

The animal study was approved by the Institutional Animal Care and Use Committee, Sun Yat-Sen University (YSU-IACUC-2018-000246).

Data availability

The data that support the findings of this study are available from the corresponding author upon reasonable request.

CRediT authorship contribution statement

Tao Yang: Conceptualization, Investigation, Methodology, Validation, Formal analysis, Data curation, Visualization, Funding acquisition, Writing – original draft. **Zhichao Hao:** Methodology, Formal analysis, Data curation, Software, Writing – review & editing. **Zhenzhen Wu:** Conceptualization, Investigation, Methodology, Data curation, Visualization, Funding acquisition, Writing – original draft. **Binxin Xu:** Methodology, Data curation, Formal analysis, Investigation. **Jiangchen Liu:** Visualization, Software. **Le Fan:** Investigation, Methodology. **Qinmei Wang:** Investigation, Methodology. **Yanshan Li:** Methodology, Formal analysis. **Dongying Li:** Methodology. **Sangzhu Tang:** Methodology. **Chuanzi Liu:** Methodology. **Weichang Li:** Conceptualization, Validation, Resources, Writing – review & editing, Supervision. **Wei Teng:** Conceptualization, Validation, Resources, Writing – review & editing, Supervision, Project administration.

Declaration of competing interest

The authors declare that they have no known competing financial interests or personal relationships that could have appeared to influence the work reported in this paper.

Acknowledgments

This research was funded by National Natural Science Foundation of China (Grant No. 82001094 and 21905094), Guangzhou Science and Technology Program (Grant No. 202102020519 and 202201010912), Guangdong Financial Fund for High-Caliber Hospital Construction (Grant No. 174-2018-XMZC-0001-03-0125/D-20), Open Funding of Guangdong Provincial Key Laboratory of Stomatology (No. KF2022120104), Guangdong Basic and Applied Basic Research Foundation (Grant No. 2019A1515110379 and 2021A1515010782).

Appendix A. Supplementary data

Supplementary data to this article can be found online at https://doi.org/10.1016/j.bioactmat.2023.03.024.

References

[1] N. Reznikov, R. Shahar, S. Weiner, Bone hierarchical structure in three dimensions, Acta Biomater. 10 (9) (2014) 3815–3826.
[2] U.G.K. Wegst, H. Bai, E. Saiz, A.P. Tomsia, R.O. Ritchie, Bioinspired structural materials, Nat. Mater. 14 (1) (2015) 23–36.
[3] Y. Du, J.L. Guo, J. Wang, A.G. Mikos, S. Zhang, Hierarchically designed bone scaffolds: from internal cues to external stimuli, Biomaterials (2019) 218.
[4] C. Piard, H. Baker, T. Kamalitdinov, J. Fisher, Bioprinted osteon-like scaffolds enhance in vivo neovascularization, Biofabrication 11 (2) (2019).
[5] G. Zhu, T. Zhang, M. Chen, K. Yao, X. Huang, B. Zhang, Y. Li, J. Liu, Y. Wang, Z. Zhao, Bone physiological microenvironment and healing mechanism: basis for future bone-tissue engineering scaffolds, Bioact. Mater. 6 (11) (2021) 4110–4140.
[6] Z. Wu, C. Bao, S. Zhou, T. Yang, L. Wang, M. Li, L. Li, E. Luo, Y. Yu, Y. Wang, X. Guo, X. Liu, The synergetic effect of bioactive molecule–loaded electrospun core-shell fibres for reconstruction of critical-sized calvarial bone defect—the effect of synergetic release on bone Formation, Cell Prolif. 53 (4) (2020), e12796.
[7] W. Dai, L. Zhang, Y. Yu, W. Yan, F. Zhao, Y. Fan, C. Cao, Q. Cai, X. Hu, Y. Ao, 3D bioprinting of heterogeneous constructs providing tissue-specific microenvironment based on host-guest modulated dynamic hydrogel bioink for osteochondral regeneration, Adv. Funct. Mater. 32 (23) (2022).
[8] X. Bai, M. Gao, S. Syed, J. Zhuang, X. Xu, X.-Q. Zhang, Bioactive hydrogels for bone regeneration, Bioact. Mater. 3 (4) (2018) 401–417.
[9] Z. Hao, Z. Song, J. Huang, K. Huang, A. Panetta, Z. Gu, J. Wu, The scaffold microenvironment for stem cell based bone tissue engineering, Biomater. Sci. 5 (8) (2017) 1382–1392.
[10] Y. Liu, D. Luo, T. Wang, Hierarchical structures of bone and bioinspired bone tissue engineering, Small 12 (34) (2016) 4611–4632.
[11] Q. Song, K. Jiao, L. Tonggu, L.G. Wang, S.L. Zhang, Y.D. Yang, L. Zhang, J.H. Bian, D.X. Hao, C.Y. Wang, Y.X. Ma, D.D. Arola, L. Breschi, J.H. Chen, F.R. Tay, L.N. Niu, Contribution of biomimetic collagen-ligand interaction to intrafibrillar mineralization, Sci. Adv. 5 (3) (2019).
[12] J. Li, J.-F. Yan, Q.-Q. Wan, M.-J. Shen, Y.-X. Ma, J.-T. Gu, P. Gao, X.-Y. Tang, F. Yu, J.-H. Chen, F.R. Tay, K. Jiao, L.-N. Niu, Matrix stiffening by self-mineralizable guided bone regeneration, Acta Biomater. 125 (2021) 112–125.
[13] T. Yang, P. Xie, Z. Wu, Y. Liao, W. Chen, Z. Hao, Y. Wang, Z. Zhu, W. Teng, The injectable woven bone-like hydrogel to perform alveolar ridge preservation with adapted remodeling performance after tooth extraction, Front. Bioeng. Biotechnol. 8 (119) (2020).
[14] Y. Wang, Y. Hua, Q. Zhang, J. Yang, H. Li, Y. Li, M. Cao, Q. Cai, X. Yang, X. Zhang, Using biomimetically mineralized collagen membranes with different surface stiffness to guide regeneration of bone defects, J. Tissue Eng. Regen. Med. 12 (7) (2018) 1545–1555.
[15] M.J. Olszta, X. Cheng, S.S. Jee, R. Kumar, Y.-Y. Kim, M.J. Kaufman, E.P. Douglas, L. B. Gower, Bone structure and formation: a new perspective, Mater. Sci. Eng. R Rep. 58 (3) (2007) 77–116.
[16] F. Despang, A. Bernhardt, A. Lode, R. Dittrich, T. Hanke, S.J. Shenoy, S. Mani, A. John, M. Gelinsky, Synthesis and physicochemical, in vitro and in vivo evaluation of an anisotropic, nanocrystalline hydroxyapatite bisque scaffold with parallel-aligned pores mimicking the microstructure of cortical bone, J. Tissue Eng. Regen. Med. 9 (12) (2015) E152–E166.
[17] Y. Li, T.T. Thula, S. Jee, S.L. Perkins, C. Aparicio, E.P. Douglas, L.B. Gower, Biomimetic mineralization of woven bone-like nanocomposites: role of collagen cross-links, Biomacromolecules 13 (1) (2011) 49–59.
[18] N. Reznikov, R. Almany-Magal, R. Shahar, S. Weiner, Three-dimensional imaging of collagen fibril organization in rat circumferential lamellar bone using a dual beam electron microscope reveals ordered and disordered sub-lamellar structures, Bone 52 (2) (2013) 676–683.
[19] N. Reznikov, R. Shahar, S. Weiner, Three-dimensional structure of human lamellar bone: the presence of two different materials and new insights into the hierarchical organization, Bone 59 (2014) 93–104.
[20] M.G. Ascenzi, A.K. Roe, The osteon: the micromechanical unit of compact bone, Front. Biosci. 17 (4) (2012) 1551–1581.
[21] S. Weiner, H.D. Wagner, The material bone: structure-mechanical function relations, Annu. Rev. Mater. Sci. 28 (1) (1998) 271–298.
[22] G. Griffanti, S.N. Nazhat, Dense fibrillar collagen-based hydrogels as functional osteoid-mimicking scaffolds, Int. Mater. Rev. 65 (8) (2020) 502–521.
[23] M. Mizuno, R. Fujisawa, Y. Kuboki, Type I collagen-induced osteoblastic differentiation of bone-marrow cells mediated by collagen-alpha2beta1 integrin interaction, J. Cell. Physiol. 184 (2) (2000) 207–213.
[24] W. Yao, N.V. Manh, H. Wang, Z. Xue, Z. Xu, C. Li, Synergistic intrafibrillar/extrafibrillar mineralization of collagen scaffolds based on a biomimetic strategy to promote the regeneration of bone defects, Int. J. Nanomed. 11 (default) (2016) 2053.
[25] Y. Liu, S.A. Liu, D. Luo, Z.J. Xue, X.A. Yang, L. Cu, Y.H. Zhou, T. Wang, Hierarchically staggered nanostructure of mineralized collagen as a bone-grafting scaffold, Adv. Mater. 28 (39) (2016) 8740–8748.
[26] M. Yu, D. Luo, J. Qiao, J.S. Guo, D.Q. He, S.S. Jin, L. Tang, Y. Wang, X. Shi, J. Mao, S.J. Cui, Y. Fu, Z.X. Li, D.W. Liu, T. Zhang, C. Zhang, Z. Li, Y.S. Zhou, Y. Liu, A hierarchical bilayer architecture for complex tissue regeneration, Bioact. Mater. 10 (2022) 93–106.
[27] X. Shi, T. Fujie, A. Saito, S. Takeoka, Y. Hou, Y. Shu, M. Chen, H. Wu, A. Khademhosseini, Periosteum-mimetic structures made from freestanding microgrooved nanosheets, Adv. Mater. 26 (20) (2014) 3290–3296.
[28] P. Fratzl, Bone fracture: when the cracks begin to show, Nat. Mater. 7 (8) (2008) 610–612.
[29] H.S. Gupta, U. Stachewicz, W. Wagermaier, P. Roschger, H.D. Wagner, P. Fratzl, Mechanical modulation at the lamellar level in osteonal bone, J. Mater. Res. 21 (8) (2006) 1913–1921.
[30] H. Razi, J. Predan, F.D. Fischer, O. Kolednik, P. Fratzl, Damage tolerance of lamellar bone, Bone 130 (2020), 115102.
[31] Z. Li, T. Du, C. Ruan, X. Niu, Bioinspired mineralized collagen scaffolds for bone tissue engineering, Bioact. Mater. 6 (5) (2021) 1491–1511.
[32] H. Liu, M. Lin, X. Liu, Y. Zhang, Y. Luo, Y. Pang, H. Chen, D. Zhu, X. Zhong, S. Ma, Y. Zhao, Q. Yang, X. Zhang, Doping bioactive elements into a collagen scaffold based on synchronous self-assembly/mineralization for bone tissue engineering, Bioact. Mater. 5 (4) (2020) 844–858.
[33] A. Dewle, N. Pathak, P. Rakshasmare, A. Srivastava, Multifarious fabrication approaches of producing aligned collagen scaffolds for tissue engineering applications, ACS Biomater. Sci. Eng. 6 (2) (2020) 779–797.
[34] L. Salvatore, N. Gallo, M.L. Natali, A. Terzi, A. Sannino, M. Madaghiele, Mimicking the hierarchical organization of natural collagen: toward the development of ideal scaffolding material for tissue regeneration, Front. Bioeng. Biotechnol. 9 (2021).
[35] M. Maher, M. Castilho, Z.L. Yue, V. Glattauer, T.C. Hughes, J.A.M. Ramshaw, G. G. Wallace, Shaping collagen for engineering hard tissues: towards a printomics approach, Acta Biomater. 131 (2021) 41–61.
[36] K.A. Alberti, A.M. Hopkins, M.D. Tang-Schomer, D.L. Kaplan, Q. Xu, The behavior of neuronal cells on tendon-derived collagen sheets as potential substrates for nerve regeneration, Biomaterials 35 (11) (2014) 3551–3557.
[37] S. Ghazanfari, K.A. Alberti, Q. Xu, A. Khademhosseini, Evaluation of an elastic decellularized tendon-derived scaffold for the vascular tissue engineering application, J. Biomed. Mater. Res. 107 (6) (2019) 1225–1234.
[38] E. Ko, K. Alberti, J.S. Lee, K. Yang, Y. Jin, J. Shin, H.S. Yang, Q. Xu, S.-W. Cho, Nanostructured tendon-derived scaffolds for enhanced bone regeneration by human adipose-derived stem cells, ACS Appl. Mater. Interfaces 8 (35) (2016) 22819–22829.
[39] K.A. Alberti, C.I. Neufeld, J. Wang, Q. Xu, In vivo peripheral nerve repair using tendon-derived nerve guidance conduits, ACS Biomater. Sci. Eng. 2 (6) (2016) 937–945.
[40] K.A. Alberti, J.-Y. Sun, W.R. Illeperuma, Z. Suo, Q. Xu, Laminar tendon composites with enhanced mechanical properties, J. Mater. Sci. 50 (6) (2015) 2616–2625.
[41] K.A. Alberti, Q. Xu, Slicing, stacking and rolling: fabrication of nanostructured collagen constructs from tendon sections, Advanced Healthcare Materials 2 (6) (2013) 817–821.
[42] T. Yang, Y. Li, Y. Hong, L. Chi, C. Liu, Y. Lan, Q. Wang, Y. Yu, Q. Xu, W. Teng, The construction of biomimetic cementum through a combination of bioskiving and fluorine-containing biomineralization, Front. Bioeng. Biotechnol. 8 (341) (2020).
[43] Z. Wu, J. Zhong, Y. Yu, M. Rong, T. Yang, A rapid and convenient approach to construct porous collagen membranes via bioskiving and sonication-feasible for mineralization to induce bone regeneration, Front. Bioeng. Biotechnol. 9 (861) (2021).
[44] T. Yang, W. Xiao, W.C. Chen, L. Li, Z. Zhu, L. Sui, Effect of carboxymethyl chitosan and aging time on synthesis and storage of amorphous calcium phosphate, J. Nanosci. Nanotechnol. 16 (12) (2016) 12582–12589.
[45] Y.P. Qi, Z. Ye, A. Fok, B.N. Holmes, M. Espanol, M.P. Ginebra, C. Aparicio, Effects of molecular weight and concentration of poly(acrylic acid) on biomimetic mineralization of collagen, ACS Biomater. Sci. Eng. 4 (8) (2018) 2758–2766.
[46] A. Vajgel, N. Mardas, B.C. Farias, A. Petrie, R. Cimões, N. Donos, A systematic review on the critical size defect model, Clin. Oral Implants Res. 25 (8) (2014) 879–893.
[47] Z.Z. Zyman, D.V. Rokhmistrov, V.I. Glushko, I.G. Ivanov, Thermal impurity reactions and structural changes in slightly carbonated hydroxyapatite, J. Mater. Sci. Mater. Med. 20 (7) (2009) 1389–1399.
[48] D. Tadic, F. Peters, M. Epple, Continuous synthesis of amorphous carbonated apatites, Biomaterials 23 (12) (2002) 2553–2559.
[49] Y. Xiao, H. Donnelly, M. Sprott, J. Luo, V. Jayawarna, L. Lemgruber, P. M. Tsimbouri, R.M.D. Meek, M. Salmeron-Sanchez, M.J. Dalby, Material-driven fibronectin and vitronectin assembly enhances BMP-2 presentation and osteogenesis, Mater Today Bio 16 (2022), 100367.
[50] R.K. Singh, D.S. Yoon, N. Mandakhbayar, C. Li, A.G. Kurian, N.-H. Lee, J.-H. Lee, H.-W. Kim, Diabetic bone regeneration with nanoceria-tailored scaffolds by recapitulating cellular microenvironment: activating integrin/TGF-β co-signaling of MSCs while relieving oxidative stress, Biomaterials 288 (2022), 121732.
[51] B. Wingender, Y. Ni, Y. Zhang, C. Taylor, L. Gower, Hierarchical characterization and nanomechanical assessment of biomimetic scaffolds mimicking lamellar bone via atomic force microscopy cantilever-based nanoindentation, Materials 11 (7) (2018) 1257.
[52] B. Wingender, P. Bradley, N. Saxena, J.W. Ruberti, L. Gower, Biomimetic organization of collagen matrices to template bone-like microstructures, Matrix Biol. 52–54 (2016) 384–396.
[53] N. Saeidi, K.P. Karmelek, J.A. Paten, R. Zareian, E. DiMasi, J.W. Ruberti, Molecular crowding of collagen: a pathway to produce highly-organized collagenous structures, Biomaterials 33 (30) (2012) 7366–7374.
[54] T. Yamamoto, T. Hasegawa, H. Hongo, N. Amizuka, Alternating lamellar structure in human cellular cementum and rat compact bone: its structure and formation, J. Oral Biosci. 61 (2) (2019) 105–114.
[55] S. Wang, Y. Wang, L. Song, J. Chen, Y. Ma, Y. Chen, S. Fan, M. Su, X. Lin, Decellularized tendon as a prospective scaffold for tendon repair, Mater Sci Eng C Mater Biol Appl 77 (2017) 1290–1301.
[56] A. Lohan, B. Kohl, C. Meier, G. Schulze-Tanzil, Tenogenesis of decellularized porcine achilles tendon matrix reseeded with human tenocytes in the nude mice xenograft model, Int. J. Mol. Sci. 19 (7) (2018).

[57] J. Wang, Q. Liu, Z. Guo, H. Pan, Z. Liu, R. Tang, Progress on Biomimetic Mineralization and Materials for Hard Tissue Regeneration, ACS biomaterials science & engineering, 2021.
[58] Y. Liu, D. Luo, S. Liu, Y. Fu, X.X. Kou, X.D. Wang, Y.L. Sha, Y.H. Gan, Y.H. Zhou, Effect of nanostructure of mineralized collagen scaffolds on their physical properties and osteogenic potential, J. Biomed. Nanotechnol. 10 (6) (2014) 1049–1060.
[59] L.N. Niu, S.E. Jee, K. Jiao, L. Tonggu, M. Li, L. Wang, Y.D. Yang, J.H. Bian, L. Breschi, S.S. Jang, J.H. Chen, D.H. Pashley, F.R. Tay, Collagen intrafibrillar mineralization as a result of the balance between osmotic equilibrium and electroneutrality, Nat. Mater. 16 (3) (2017) 370–378.
[60] M.L. Lin, H.H. Liu, J.J. Deng, R. An, M.J. Shen, Y.Q. Li, X. Zhang, Carboxymethyl chitosan as a polyampholyte mediating intrafibrillar mineralization of collagen via collagen/ACP self-assembly, J. Mater. Sci. Technol. 35 (9) (2019) 1894–1905.
[61] S. Karthika, T. Radhakrishnan, P. Kalaichelvi, A review of classical and nonclassical nucleation theories, Cryst. Growth Des. 16 (11) (2016) 6663–6681.
[62] M.M. Giraud-Guille, Twisted plywood architecture of collagen fibrils in human compact bone osteons, Calcif. Tissue Int. 42 (3) (1988) 167–180.
[63] P. Vashisth, J.R. Bellare, Development of hybrid scaffold with biomimetic 3D architecture for bone regeneration, Nanomed. Nanotechnol. Biol. Med. 14 (4) (2018) 1325–1336.
[64] C.E. Hoffler, K.E. Moore, K. Kozloff, P.K. Zysset, M.B. Brown, S.A. Goldstein, Heterogeneity of bone lamellar-level elastic moduli, Bone 26 (6) (2000) 603–609.
[65] Y. Shen, D. Jing, Z. Zhao, The effect of AKT in extracellular matrix stiffness induced osteogenic differentiation of hBMSCs, Cell. Signal. (2022), 110404, 110404.
[66] M. Sun, G. Chi, J. Xu, Y. Tan, J. Xu, S. Lv, Z. Xu, Y. Xia, L. Li, Y. Li, Extracellular matrix stiffness controls osteogenic differentiation of mesenchymal stem cells mediated by integrin alpha 5, Stem Cell Res. Ther. 9 (2018).
[67] H. Zheng, Y. Tian, Q. Gao, Y. Yu, X. Xia, Z. Feng, F. Dong, X. Wu, L. Sui, Hierarchical micro-nano topography promotes cell adhesion and osteogenic differentiation via integrin alpha 2-PI3K-AKT signaling Axis, Front. Bioeng. Biotechnol. 8 (2020).
[68] J.P. Schmitz, J.O. Hollinger, The critical size defect as an experimental model for craniomandibulofacial nonunions, Clin. Orthop. Relat. Res. 205 (1986) 299–308.
[69] T. Fernandez, G. Olave, C.H. Valencia, S. Arce, J.M.W. Quinn, G.A. Thouas, Q. Z. Chen, Effects of calcium phosphate/chitosan composite on bone healing in rats: calcium phosphate induces osteon formation, Tissue Eng. 20 (13–14) (2014) 1948–1960.
[70] K. Nettleton, D. Luong, A.P. Kleinfehn, L. Savariau, C. Premanandan, M.L. Becker, Molecular mass-dependent resorption and bone regeneration of 3D printed PPF scaffolds in a critical-sized rat cranial defect model, Adv Healthc Mater 8 (17) (2019), e1900646.
[71] H. Toker, H. Ozdemir, H. Ozer, K. Eren, A comparative evaluation of the systemic and local alendronate treatment in synthetic bone graft: a histologic and histomorphometric study in a rat calvarial defect model, Oral Surg Oral Med Oral Pathol Oral Radiol 114 (5 Suppl) (2012) S146–S152.